STh-01

MODERN ADVANCES IN COMPUTATIONAL IMAGING AT MICROWAVE AND MILLIMETRE-WAVE FREQUENCIES

Okan Yurduseven[#1], Thomas Fromentèze[#2]

[#1]Queen’s University Belfast, UK

[#2]Xlim Research Institute, University of Limoges, France

[1]okan.yurduseven@qub.ac.uk, [2]thomas.fromenteze@unilim.fr

EuMW 2019
UNIVERSALITY THROUGH MICROWAVES

EUROPEAN MICROWAVE WEEK 2019
SIX DAYS · THREE CONFERENCES · ONE EXHIBITION
PORTE DE VERSAILLES PARIS, FRANCE
29TH SEPTEMBER - 4TH OCTOBER 2019

Exhibition Hours:
Tuesday, 1st October 9.30 - 18.00
Wednesday 2nd October 9.30 - 17.30
Thursday 3rd October 9.30 - 16.30
www.eumweek.com

STh-01

New advances in computational imaging: Polarimetric imaging, phaseless imaging, and recent advances in antenna systems and k-space reconstruction techniques

Okan Yurduseven[#1], Thomas Fromenteze[#2]

[#1]Queen’s University Belfast, UK

[#2]Xlim Research Institute, University of Limoges, France

[1]okan.yurduseven@qub.ac.uk, [2]thomas.fromenteze@unilim.fr

Outlines of the second part

- Acceleration of image reconstruction: k-space and Fourier processing
- Computational polarimetric imaging
- Computational phaseless imaging

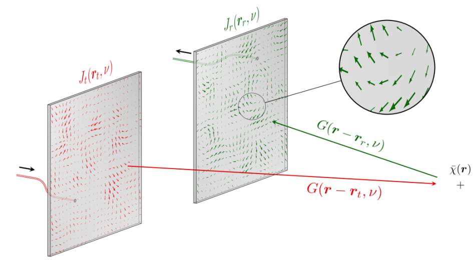

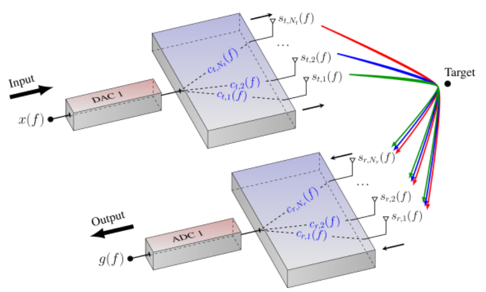

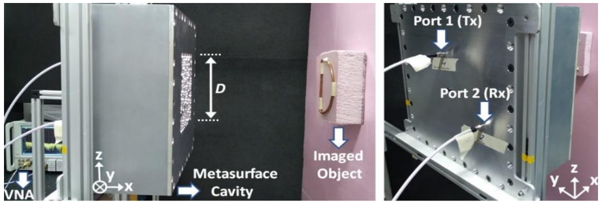

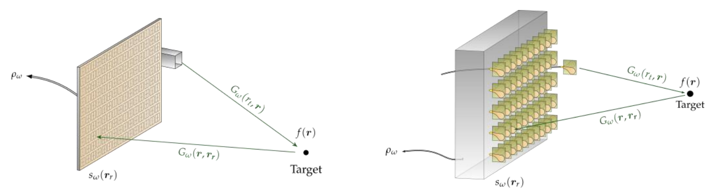

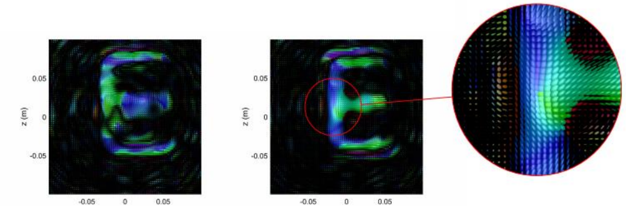

Accelerating computational imaging with Fourier processing

Some problems require the estimation of millions of voxels

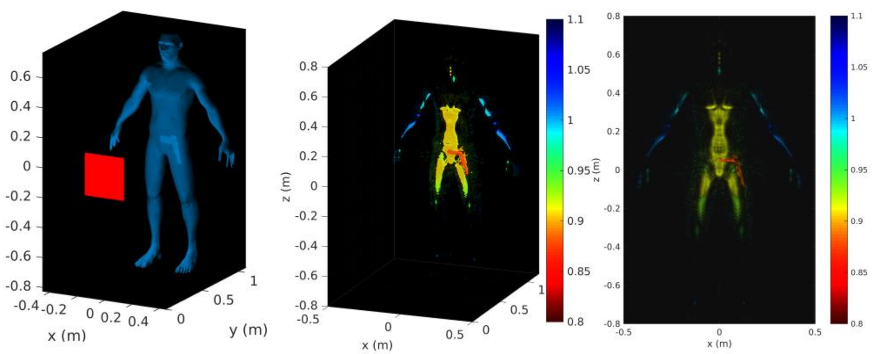

Using MIMO apertures, the number of measured samples can also reach very large numbers

Sensing matrix

Transmitters × Receivers × Frequency samples

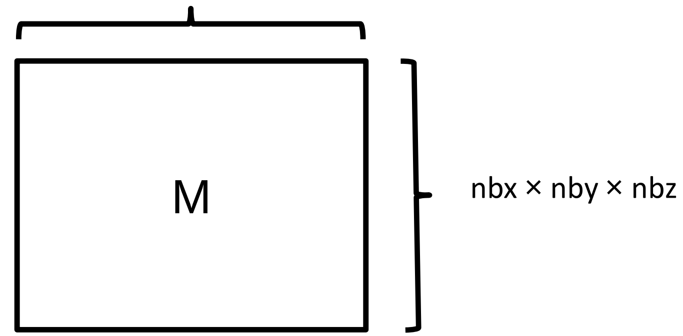

Example

Transmitters : 40 × 40
Receivers : 40 × 40
Frequency points : 20
nbx : 300
nby : 200
nbz : 300

size(H) = $51.10^6 \times 18.10^6$

Raw memory consumption
~2200 Tb (single precision)

Fromenteze, T., Yurduseven, O., Berland, F., Decroze, C., Smith, D. R., & Yarovoy, A. G. (2019). A Transverse Spectrum Deconvolution Technique for MIMO Short-Range Fourier Imaging. *IEEE Transactions on Geoscience and Remote Sensing*.

What makes Fourier processing so efficient?

Propagation is modelled within a scalar model: waves progress from source points in a spherical manner.

$$G(r, r_a) = \frac{e^{-jk|r-r_a|}}{|r-r_a|}$$

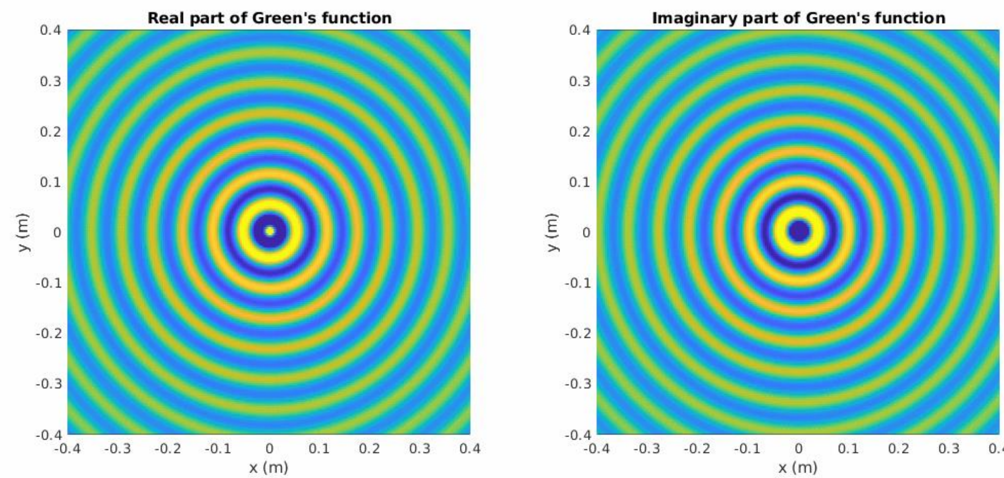

Note: Explanations are given for a set of 2D examples. For the sake of simplicity, we use an asymptotic form of Hankel's functions: $H_0^{(2)}(kr) \approx \frac{e^{-jkr}}{\sqrt{r}}$

What makes Fourier processing so efficient?

Following an angular spectrum decomposition, a spherical wave is analogous to a sum of plane waves

Weyl's expansion:

$$\frac{e^{jkr}}{r} = \frac{j}{2\pi} \iint e^{j(k_x x + k_z z + |k_y| y)}\, dk_x dk_z$$

with: $k_y = \sqrt{k^2 - k_x^2 - k_z^2}$

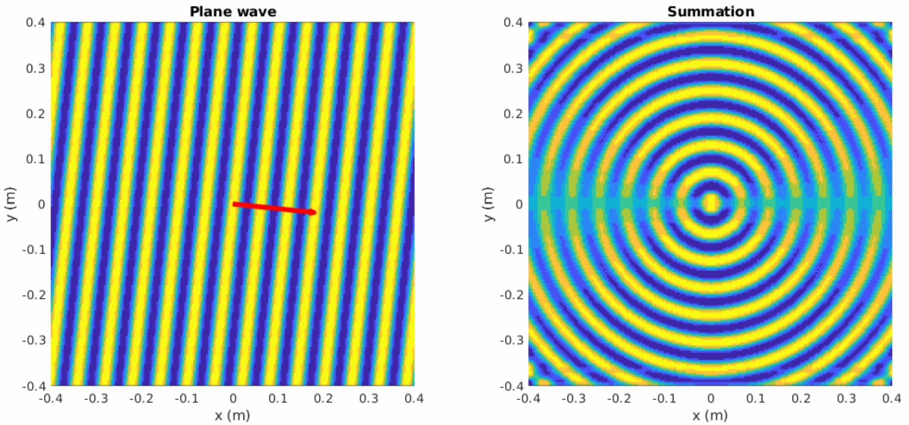

What makes Fourier processing so efficient?

Impact of a spatial Fourier transform on measurements:

$$S(k_x, f) = \mathfrak{F}(S(x, f))$$

The transformation helps to identify a set of angles of arrival

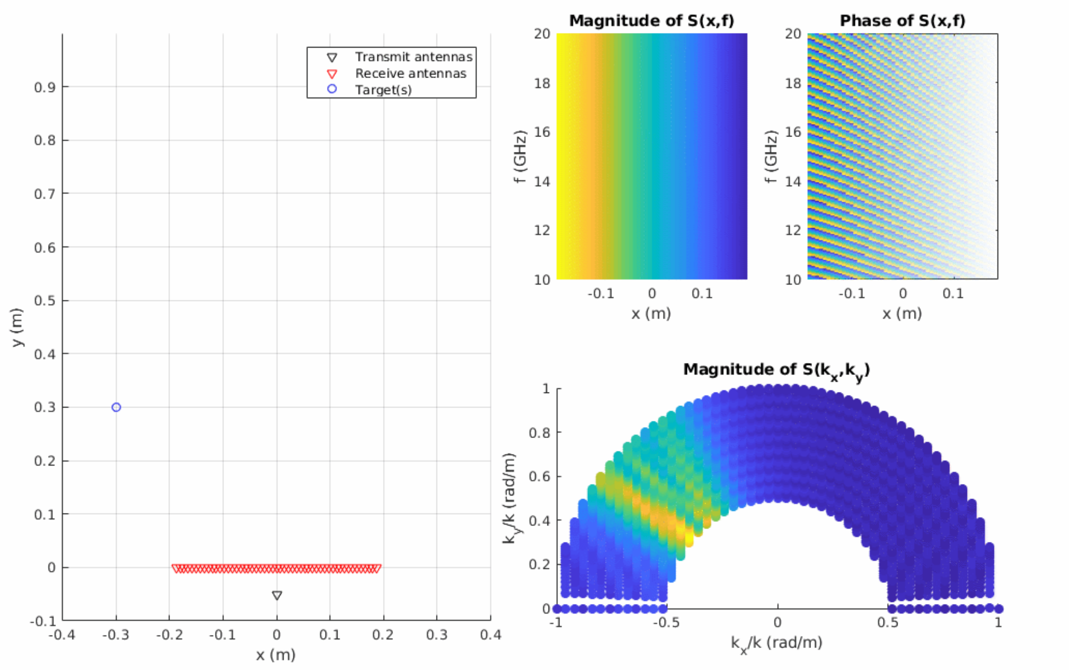

What makes Fourier processing so efficient?

Impact of a spatial Fourier transform on measurements:

$$S(k_x, f) = \mathfrak{F}(S(x, f))$$

The transformation helps to identify a set of angles of arrival

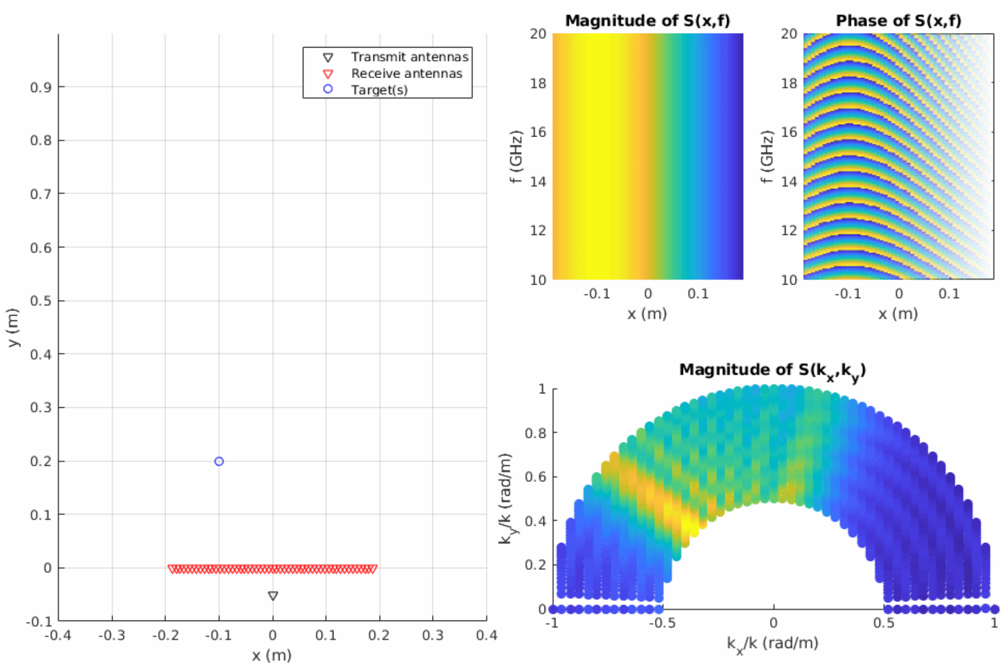

What makes Fourier processing so efficient?

A fundamental concept for short-range Fourier imaging: **the definition of a dispersion relation**

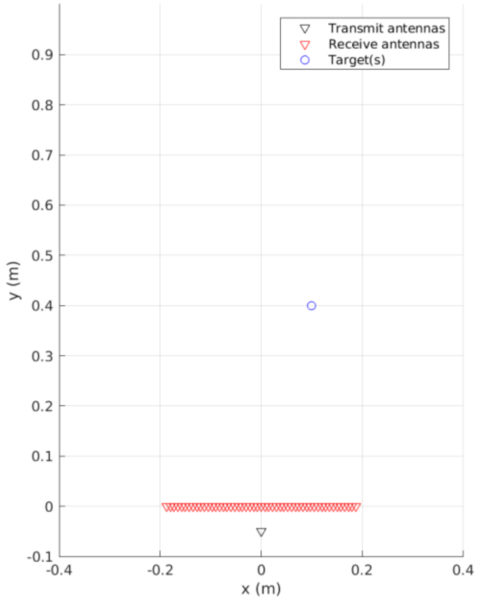

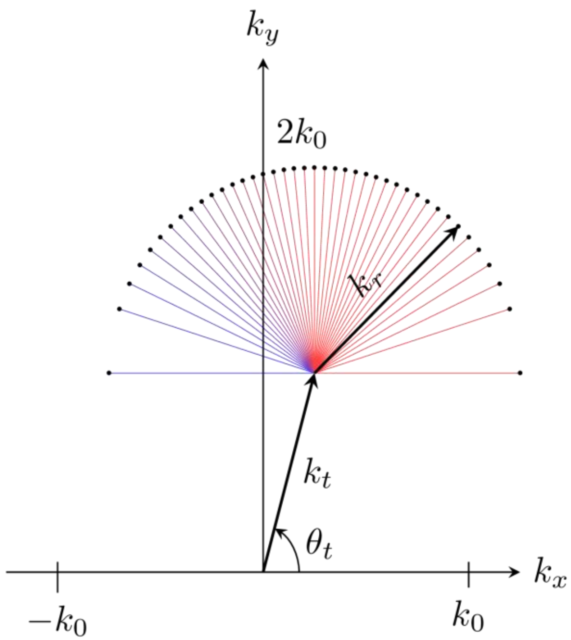

An association of transmitted and received plane waves are considered:

$$k_y = k_t + k_r$$

In the SIMO case:
A single Tx plane wave interacts with a set of Rx plane waves

$$k_y = k\sin(\theta_t) + \sqrt{k^2 - k_x^2}$$

We choose an area to image whose center is called the **stationary phase point.**

Product of Tx and Rx Green's functions: sum of the arguments of their exponential functions (the rigorous demonstration is not that straightforward)

What makes Fourier processing so efficient?

Code available here
https://bit.ly/2XGCVbH

Full process for image computation:

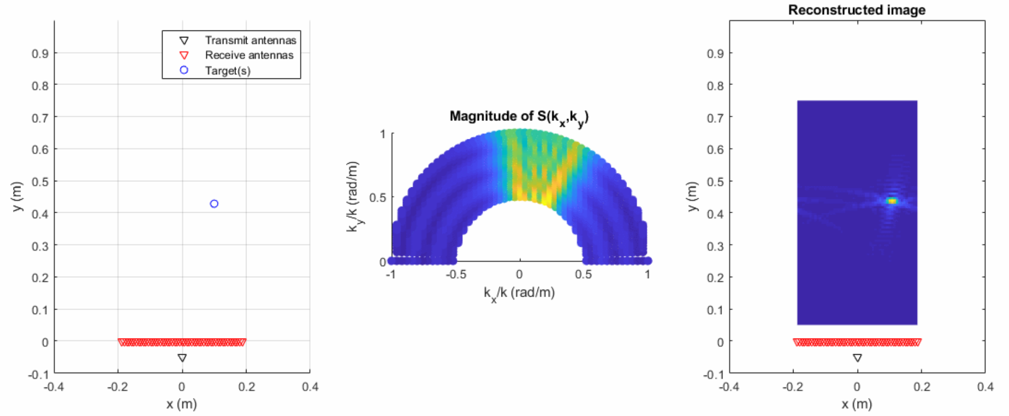

1. Fourier transform and variable change

$$S(x,f) \longrightarrow S(k_x,f) \xrightarrow{k=\frac{2\pi f}{c}} S(k_x,k)$$

2. Back-propagation

$$S(k_x,y) = \int S(k_x,k)\, e^{j\overbrace{\left(k+\sqrt{k^2-k_x^2}\right)}^{k_y} y}\, dk$$

3. Inverse Fourier transform

$$I(x,y) = \mathfrak{F}^{-1}(S(k_x,y))$$

This approach is often referred as the **Range Migration Algorithm** (RMA) or k-ω algorithm

Lopez-Sanchez, J. M., & Fortuny-Guasch, J. (2000). 3-D radar imaging using range migration techniques. *IEEE Transactions on antennas and propagation*, *48*(5), 728-737.

Zhuge, X., & Yarovoy, A. G. (2012). Three-dimensional near-field MIMO array imaging using range migration techniques. *IEEE Transactions on Image Processing*, *21*(6), 3026-3033.

Note:
1. The back-propagation step can be greatly accelerated using Stolt interpolation instead of a summation.
2. In this example, we add an additional phase shift $e^{jk\Delta y}$ to compensate for the offset of the transmit antenna.

Making Fourier techniques compatible with computational imaging

Problem: the use of frequency-diverse antenna does not grant us direct access to the spatial dimension

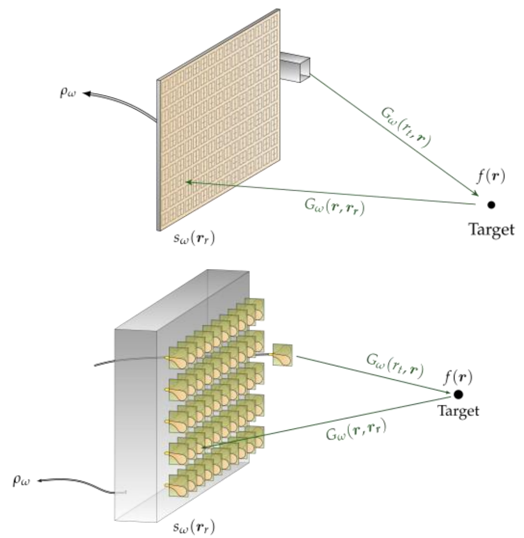

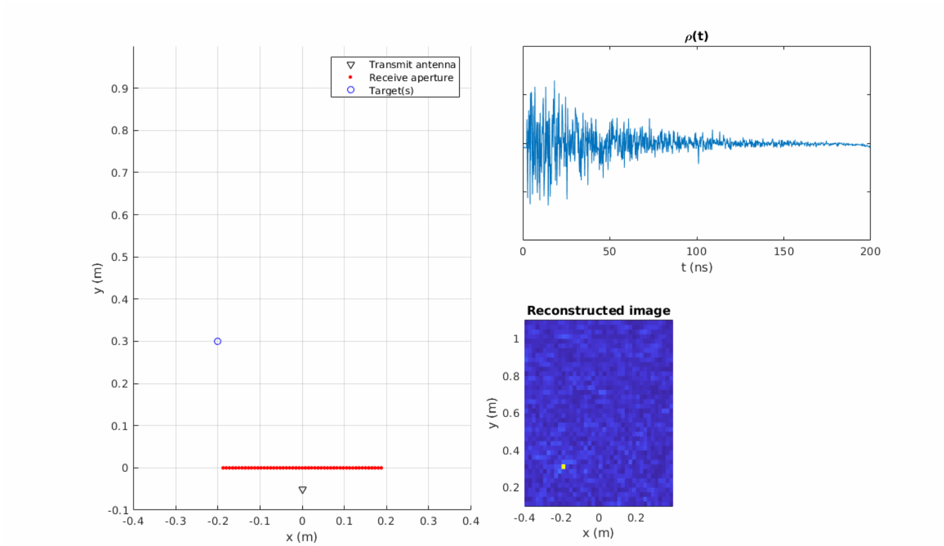

Measurement of a "compressed" signal:

$$\rho_\omega = \int_{r_r} \int_r G_\omega(r_t, r) f(r) G_\omega(r, r_r)\ d^3r\ H_\omega(r_r) d^2 r_r$$

Identification of signals in the radiating aperture

$$s_\omega(r_r) = \int_r G_\omega(r_t, r) f(r) G_\omega(r, r_r)\ d^3r$$

How to efficiently retrieve the signals in the aperture?

Making Fourier techniques compatible with computational imaging

Problem: the use of frequency-diverse antenna does not grant us direct access to the spatial dimension

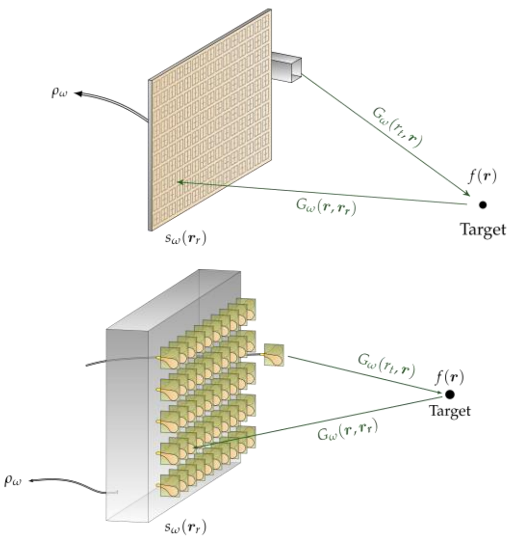

Measurement of a "compressed" signal

$$\rho_\omega = \int_{r_r} \int_r G_\omega(r_t, r) f(r) G_\omega(r, r_r)\ d^3 r\ H_\omega(r_r) d^2 r_r$$

Identification of signals in the radiating aperture

$$s_\omega(r_r) = \int_r G_\omega(r_t, r) f(r) G_\omega(r, r_r)\ d^3 r$$

The signals undergo a known distortion

$$\rho_\omega = \int_{r_r} s_\omega(r_r)\ H_\omega(r_r) d^2 r_r$$

In matrix form

$$\rho_\omega = H_\omega^T s_\omega \text{ with } \quad H_\omega \in \mathbb{C}^{n_{r_r} \times 1}, \quad s_\omega \in \mathbb{C}^{n_{r_r} \times 1}$$

Problem: a simple matrix inversion reconstruction requires the sacrifice of a dimension

$$\hat{s}_\circ = H^+ \rho \text{ with } \quad H \in \mathbb{C}^{n_f \times n_{r_r}}, \quad \rho \in \mathbb{C}^{n_f \times 1}, \quad s_\circ \in \mathbb{C}^{n_{r_r} \times 1}$$

Pros: we just retrieved our lost spatial dimension

Cons: our frequency dimension is now missing

Making Fourier techniques compatible with computational imaging

Problem: the use of frequency-diverse antenna does not grant us direct access to the spatial dimension

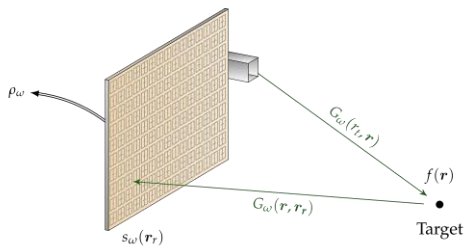

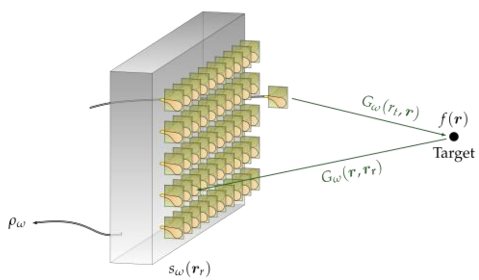

The measurement can also be written as a **Hadamard product** (element-wise multiplication)

$$\rho = \sum_{r_r} H \odot s \quad \text{with} \quad H \in \mathbb{C}^{n_f \times n_{r_r}}, \quad s \in \mathbb{C}^{n_f \times n_{r_r}}$$

An estimation is carried out using an **equalization**

$$\hat{s}_{eq} = H^+ \odot (\rho, \dots, \rho)$$

The measured "compressed" signal is multiplied by each line of the pseudo-inverse matrix

The signals reconstructed in the radiating aperture can finally be used to reconstruct images using Fourier techniques.

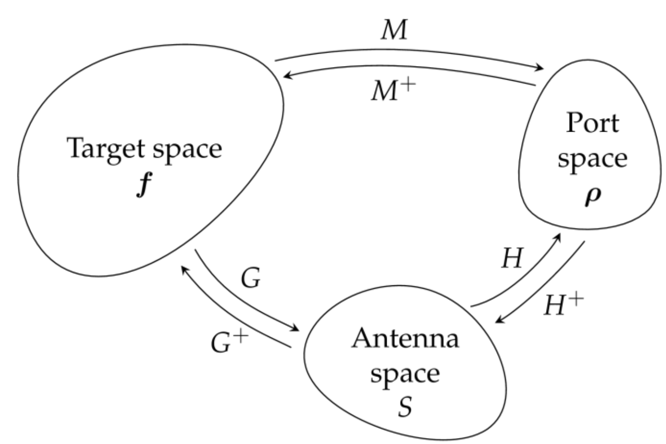

Performance comparison : Equalization+RMA VS full-matrix approach

Equalization+RMA

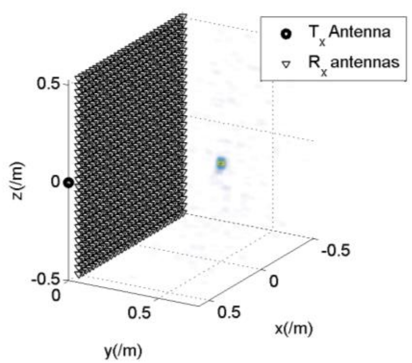

Full-matrix approach

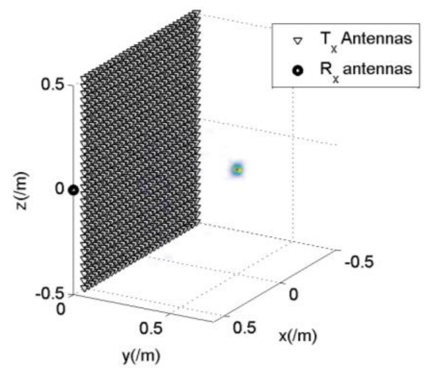

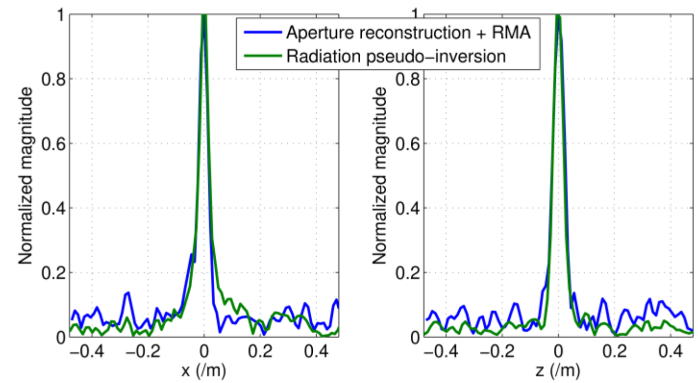

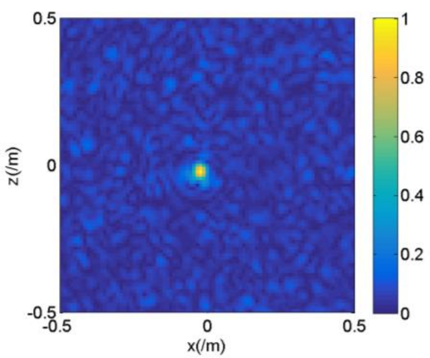

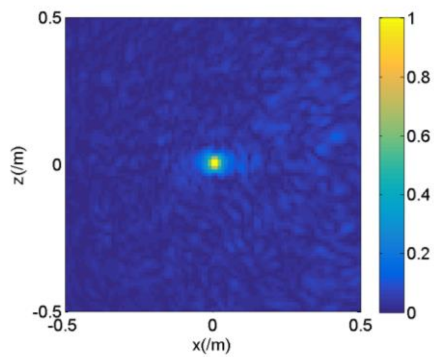

	Pre-computation time	Computation time
Eq+RMA	4.8 s	2.4 s
Full-matrix	38 min	66 s

Data presented in 2015, significant progress has been made on both methods since

Fromenteze, T., Kpré, E. L., Decroze, C., Carsenat, D., Yurduseven, O., Imani, M., ... & Smith, D. R. (2015, September). Unification of compressed imaging techniques in the microwave range and deconvolution strategy. In *2015 European Radar Conference (EuRAD)* (pp. 161-164). IEEE.

Examples of implementations

From 4 antennas to 1 receiver

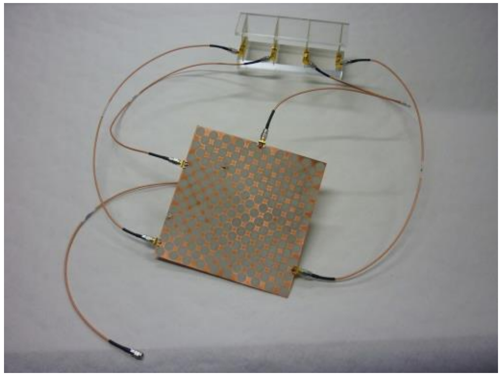

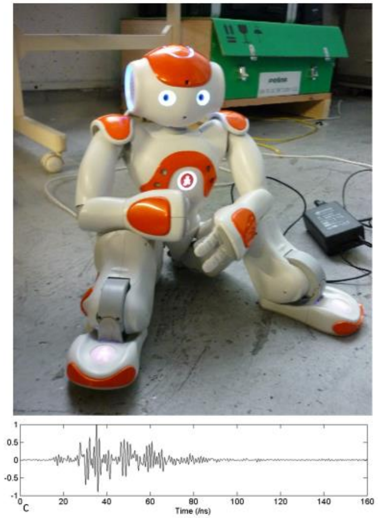

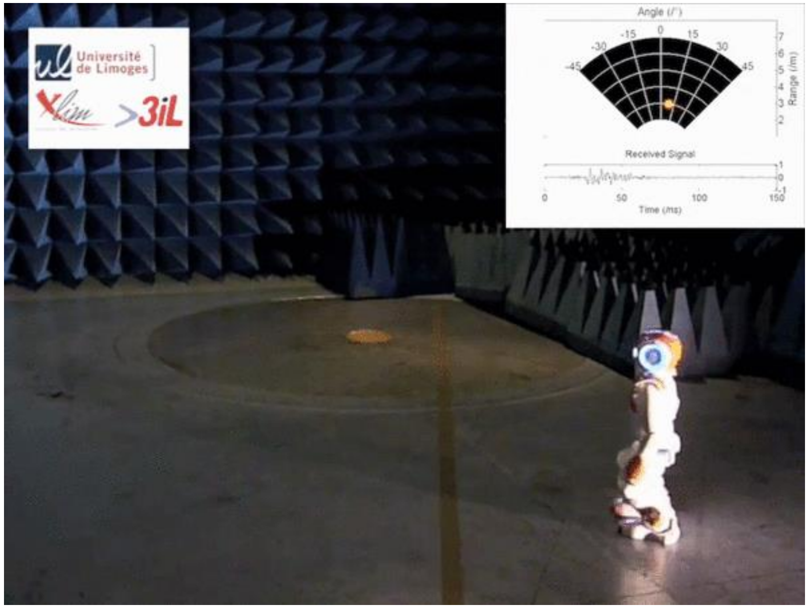

Frequency range: 2-4 GHz
7 fps (limited by communication times between equipment)

Fromenteze, T., Decroze, C., & Carsenat, D. (2014). Waveform coding for passive multiplexing: Application to microwave imaging. *IEEE Transactions on Antennas and Propagation*, *63*(2), 593-600.

Examples of implementations

From 16 antennas to 4 receivers

Frequency range: 2-4 GHz

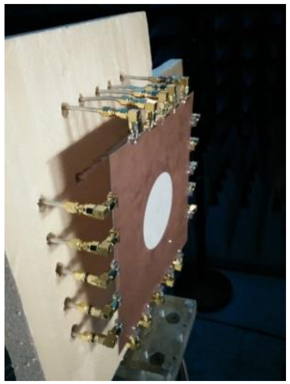

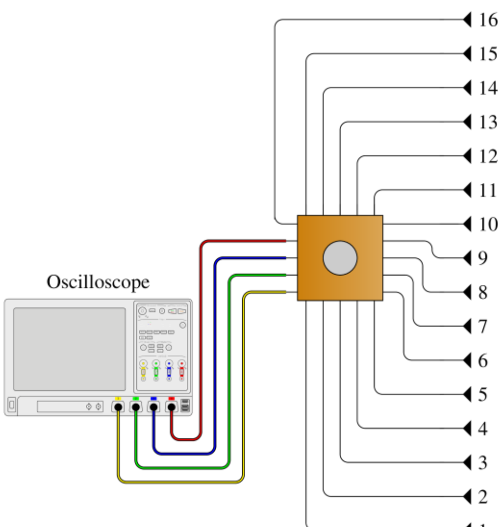

Improvement of the equalization technique by a sparsity-driven technique based on Toeplitz matrices

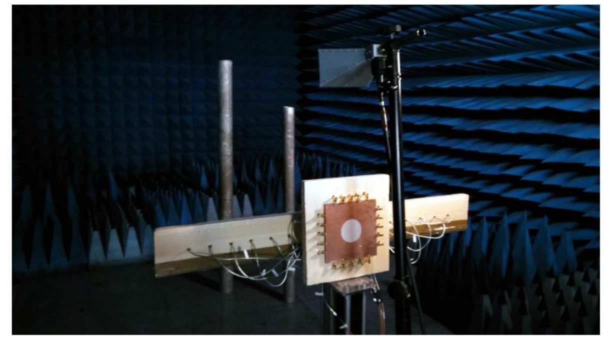

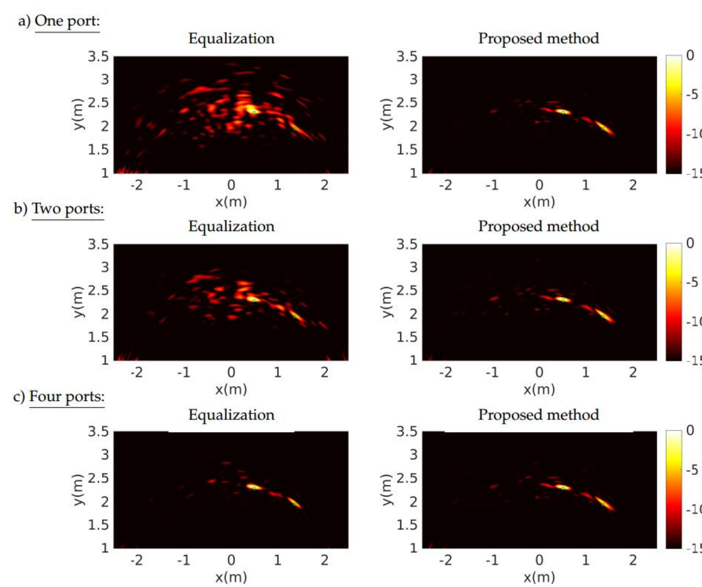

Fromenteze, T., Kpré, E. L., Decroze, C., & Carsenat, D. (2015, September). Passive UWB beamforming: AN to M compression study. In *2015 European Radar Conference (EuRAD)* (pp. 169-172). IEEE.

Fromenteze, T., Decroze, C., Abid, S., & Yurduseven, O. (2018). Sparsity-Driven Reconstruction Technique for Microwave/Millimeter-Wave Computational Imaging. *Sensors*, *18*(5), 1536.

Examples of implementations

Going MIMO:
From 24x24 antennas to 1 transceiver

Frequency range: 2-10 GHz

Image computation:
1.5 s with MIMO RMA

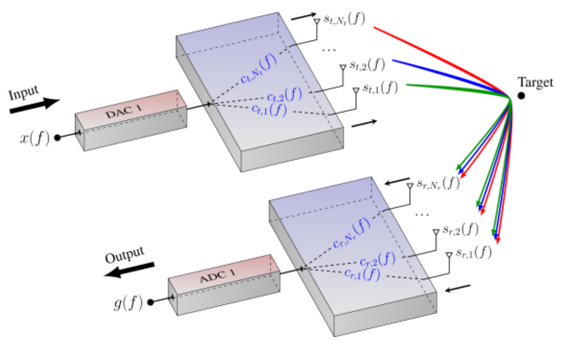

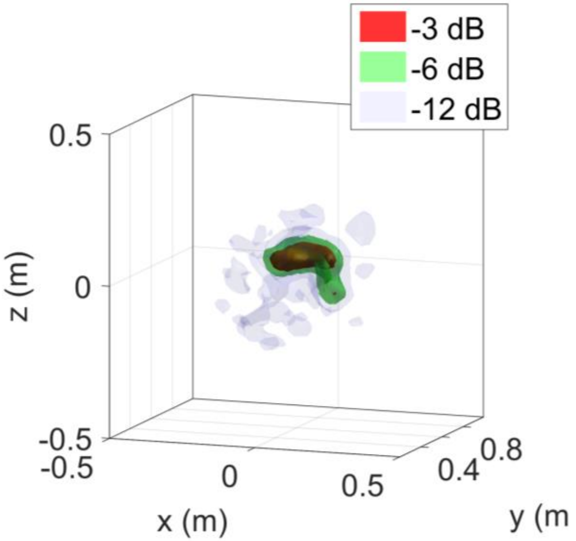

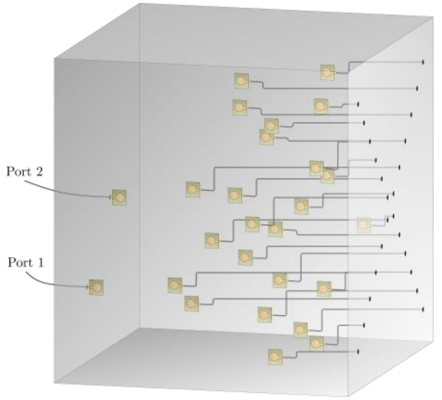

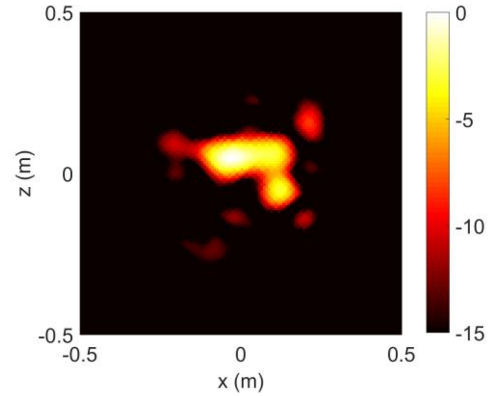

Fromenteze, T., Kpré, E. L., Carsenat, D., Decroze, C., & Sakamoto, T. (2016). Single-shot compressive multiple-inputs multiple-outputs radar imaging using a two-port passive device. *IEEE Access*, *4*, 1050-1060.

Improving the MIMO RMA

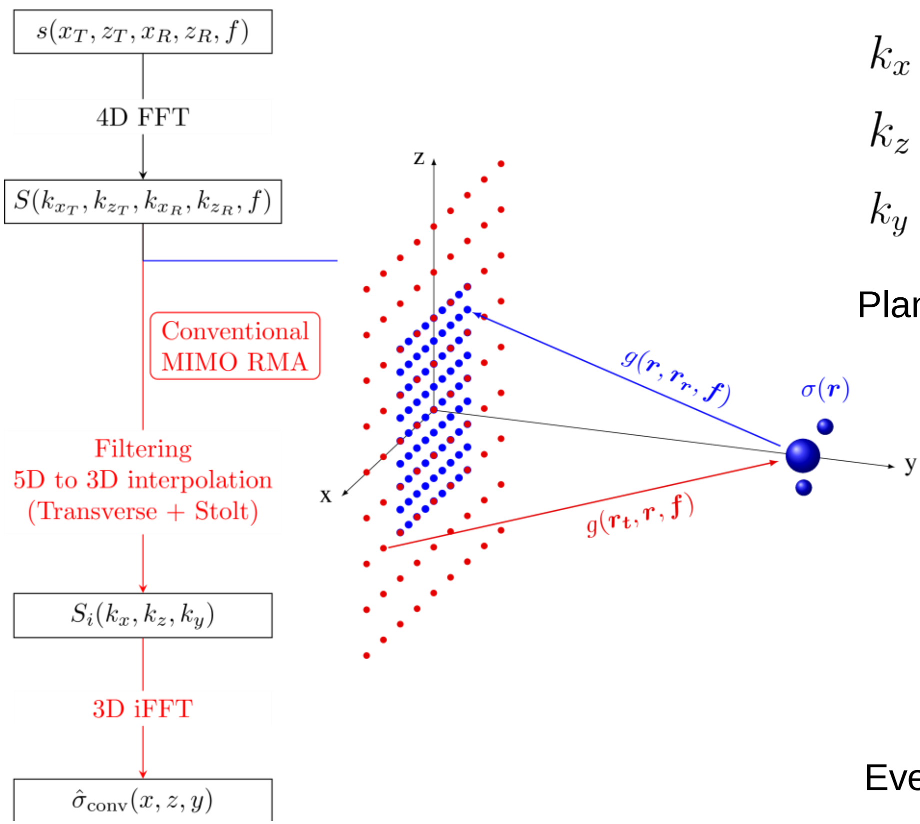

Bottleneck of the RMA:
interpolating the Tx and Rx plane waves

$$k_x = k_{x_T} + k_{x_R}$$
$$k_z = k_{z_T} + k_{z_R}$$
$$k_y = \sqrt{k^2 - k_{x_T}^2 - k_{z_T}^2} + \sqrt{k^2 - k_{x_R}^2 - k_{z_R}^2}$$

Plane wave fusion can be computationally intensive

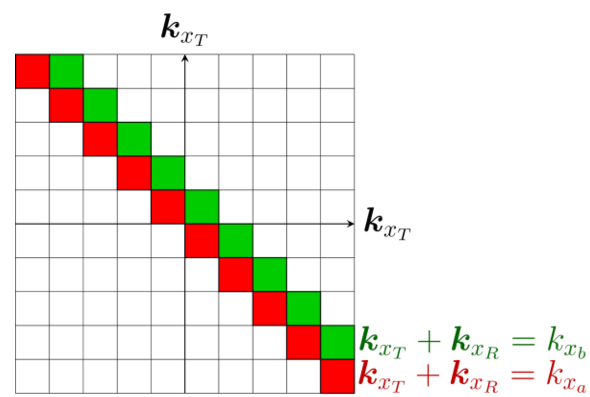

Everything else can be done from Fast-Fourier transforms

$$\hat{\sigma}(x,y,z) = k_{y_T} k_{y_R} \int_{k_x} \int_{k_y} \int_{k_z} S(k_{x_T}, k_{z_T}, k_{x_R}, k_{z_R}, k) e^{jk_y y} e^{jk_x x} e^{jk_z z} dk_x dk_y dk_z$$

Fromenteze, T., Yurduseven, O., Berland, F., Decroze, C., Smith, D. R., & Yarovoy, A. G. (2019). A Transverse Spectrum Deconvolution Technique for MIMO Short-Range Fourier Imaging. *IEEE Transactions on Geoscience and Remote Sensing*.

Improving the MIMO RMA

The initial approach is quite abstract and based on asymptotic developments of radiation integrals

To the authors' knowledge, all asymptotic developments proposed in this field are based on a simplified derivation of the measured signals, considering that amplitude terms have a negligible usefulness in comparison with phase terms and can thus be removed. It is shown in this section that it is necessary to keep the decay term $1/R$, evaluated at the stationary phase point so that the final expression converges towards a form very close to that given in the references mentioned above. From a physical point of view, the conservation of the amplitude term also seems justified insofar as this information remains of particular interest in the context of imaging applications in the Fresnel zone.

We start the calculations from the initial formalism of the MIMO signal simplified according to a scalar field approximation and to first-order Born approximation.

$$s(x_t, z_t, x_r, z_r, k) = \int_r \frac{\sigma(r)}{16\pi^2} \frac{e^{-jkR_t}}{R_t} \frac{e^{-jkR_r}}{R_r} d^3r \qquad (1)$$

with

$$R_t = \sqrt{(x - x_t)^2 + y^2 + (z - z_t)^2} \qquad (2)$$
$$R_r = \sqrt{(x - x_r)^2 + y^2 + (z - z_r)^2} \qquad (3)$$
$$R = \sqrt{x^2 + y^2 + z^2} \qquad (4)$$
$$dV = \partial x\, \partial y\, \partial z \qquad (5)$$

The spatial dimensions are expressed in the Fourier domain in order to consider the interaction between the emitted and received plane waves and the target to be imaged.

$$S(k_{x_t}, k_{z_t}, k_{x_r}, k_{z_r}, k) = \mathfrak{F}_{4D}\big(s(x_t, z_t, x_r, z_r, k)\big) \qquad (6)$$

The development of the expression of this signal makes it possible to factorize the transmission and reception terms.

$$S = \int_r \int_{A_t} \int_{A_r} \frac{\sigma(r)}{16\pi^2} \frac{e^{-jkR_t}}{R_t} \frac{e^{-jkR_r}}{R_r} e^{-jk_{x_t}x_t} e^{-jk_{z_t}z_t} e^{-jk_{x_r}x_r} e^{-jk_{z_r}z_r}\, dA_r\, dA_t\, d^3r \qquad (7)$$

$$= \int_r \frac{\sigma(r)}{16\pi^2} \Big[\underbrace{\int_{A_t} \frac{e^{-jkR_t}}{R_t} e^{-jk_{x_t}x_t} e^{-jk_{z_t}z_t}\, dA_t}_{E_t}\Big] \Big[\underbrace{\int_{A_r} \frac{e^{-jkR_r}}{R_r} e^{-jk_{x_r}x_r} e^{-jk_{z_r}z_r}\, dA_r}_{E_r}\Big] d^3r \qquad (8)$$

where the surface elements of the transmit and receive apertures are respectively $dA_t = \partial x_t \partial z_t$ and $dA_r = \partial x_r \partial z_r$. The integrals E_t and E_r share the same mathematical form that can be simplified using the method of stationary phase. These expressions are developed here with a generic index i standing for t or r:

$$E_i(k_{x_i}, k_{z_i}, k) = \int_{x_i}\int_{z_i} \frac{e^{-jkR_i}}{R_i}\, e^{-jk_{x_i}x_i} e^{-jk_{z_i}z_i} \partial x_i \partial z_i \qquad (9)$$

The evaluation of this integral is carried out using asymptotic development. It is therefore necessary to express this expression in a particular oscillatory integral form:

$$E_i(k_{x_i}, k_{z_i}, k) = \int_{x_i}\int_{z_i} \frac{e^{-jk\sqrt{(x_i-x)^2+y^2+(z_i-z)^2}}}{\sqrt{(x_i - x)^2 + y^2 + (z_i - z)^2}}\, e^{-jk_{x_i}x_i} e^{-jk_{z_i}z_i}\, \partial x_i \partial z_i \qquad (10)$$

$$= \int_{x_i}\int_{z_i} \frac{1}{R}\, e^{jk\Phi}\, \partial x_i \partial z_i \qquad (11)$$

with

$$\Phi = -\sqrt{(x_i - x)^2 + y^2 + (z_i - z)^2} - \frac{k_{x_i}}{k} x_i - \frac{k_{z_i}}{k} z_i \qquad (12)$$
$$R = \sqrt{(x_i - x)^2 + y^2 + (z_i - z)^2} \qquad (13)$$

The factorization of the wavenumber k makes it possible to introduce a phase term Φ that varies slowly with respect to the frequency. This development makes it possible to realize an asymptotic expansion of the integral, considering that the most significant contributions arises a saddle point called the stationary phase point (x_s, z_s), and defined as:

$$\frac{\partial\Phi}{\partial x_i}\Big|_{x_s,z_s} = 0 \qquad (14)$$
$$\frac{\partial\Phi}{\partial z_i}\Big|_{x_s,z_s} = 0 \qquad (15)$$

A second order 2D Taylor expansion of Φ is calculated at the stationary phase point $(x_i = x_s, z_i = z_s)$:

$$\begin{aligned}\Phi \approx\; & \Phi(x_s, z_s) + \overbrace{\frac{\partial\Phi}{\partial x_i}\Big|_{x_s,z_s}}^{=0}(x_i - x_s) + \overbrace{\frac{\partial\Phi}{\partial z_i}\Big|_{x_s,z_s}}^{=0}(z_i - z_s) \\ & + \frac{\partial^2\Phi}{\partial x_i^2}\Big|_{x_s,z_s}\frac{(x_i - x_s)^2}{2!} + \frac{\partial^2\Phi}{\partial z_i^2}\Big|_{x_s,z_s}\frac{(z_i - z_s)^2}{2!} \\ & + \frac{1}{2!}\frac{\partial^2\Phi}{\partial x_i \partial z_i}\Big|_{x_s,z_s}(x_i - x_s)(z_i - z_s) \\ & + \frac{1}{2!}\frac{\partial^2\Phi}{\partial z_i \partial x_i}\Big|_{x_s,z_s}(x_i - x_s)(z_i - z_s)\end{aligned} \qquad (16)$$

$$\begin{aligned}\Phi \approx\; & \Phi(x_s, z_s) + \frac{\partial^2\Phi}{\partial x_i^2}\Big|_{x_s,z_s}\frac{(x_i - x_s)^2}{2!} \\ & + \frac{\partial^2\Phi}{\partial z_i^2}\Big|_{x_s,z_s}\frac{(z_i - z_s)^2}{2!} \\ & + \frac{\partial^2\Phi}{\partial x_i \partial z_i}\Big|_{x_s,z_s}(x_i - x_s)(z_i - z_s)\end{aligned} \qquad (17)$$

The expression of x_s and z_s can first be obtained from the first derivatives vanishing at the stationary phase point:

$$\frac{\partial\Phi}{\partial x_i}\Big|_{x_s,z_s} = -\frac{x_s - x}{\sqrt{(x_s - x)^2 + y^2 + (z_s - z)^2}} - \frac{k_{x_i}}{k} = 0 \qquad (18)$$

$$\frac{\partial\Phi}{\partial z_i}\Big|_{x_s,z_s} = -\frac{z_s - z}{\sqrt{(x_s - x)^2 + y^2 + (z_s - z)^2}} - \frac{k_{z_i}}{k} = 0 \qquad (19)$$

Eqs. (18) and (19) then lead to the following coupled equations:

$$(x_s - x)^2 = \frac{k_{x_i}^2}{k^2 - k_{x_i}^2}(y^2 + (z_s - z)^2) \qquad (20)$$
$$(z_s - z)^2 = \frac{k_{z_i}^2}{k^2 - k_{z_i}^2}(y^2 + (x_s - x)^2) \qquad (21)$$

The resolution of this last equation system makes it possible to determine the expression of the coordinates of the stationary phase point, extracting the positive roots for each case:

$$x_s = x + y\frac{k_{x_i}}{\sqrt{k^2 - k_{x_i}^2 - k_{z_i}^2}} \qquad (22)$$
$$z_s = z + y\frac{k_{z_i}}{\sqrt{k^2 - k_{x_i}^2 - k_{z_i}^2}} \qquad (23)$$

The second derivatives $\partial^2\Phi/\partial x_i^2$, $\partial^2\Phi/\partial z_i^2$, and $\partial^2\Phi/\partial x_i \partial z_i$ can now be evaluated, reminding that $\Phi = -\sqrt{(x_i - x)^2 + y^2 + (z_i - z)^2} - \frac{k_{x_i}}{k}x_i - \frac{k_{z_i}}{k}z_i$:

$$\frac{\partial^2\Phi}{\partial x_i^2} = \frac{\partial}{\partial x_i}\left(-\frac{x_i - x}{\sqrt{(x_i - x)^2 + y^2 + (z_i - z)^2}} - \frac{k_{x_i}}{k}\right) \qquad (24)$$

$$= \frac{y^2 + (z_i - z)^2}{((x_i - x)^2 + y^2 + (z_i - z)^2)^{\frac{3}{2}}} \qquad (25)$$

Similarly, we evaluate the second derivative of the phase term according to z_i:

$$\frac{\partial^2\Phi}{\partial z_i^2} = -\frac{y^2 + (x_i - x)^2}{((x_i - x)^2 + y^2 + (z_i - z)^2)^{\frac{3}{2}}} \qquad (26)$$

The last second derivative $\partial^2\Phi/\partial x_i \partial z_i$ is finally evaluated:

$$\frac{\partial^2\Phi}{\partial x_i \partial z_i} = \frac{\partial}{\partial x_i}\frac{\partial\Phi}{\partial z_i} = \frac{\partial}{\partial x_i}\left(-\frac{z_i - z}{\sqrt{x^2 + y^2 + z^2}} - \frac{k_{z_i}}{k}\right) \qquad (27)$$

$$\frac{\partial^2\Phi}{\partial x_i \partial z_i} = -\frac{(x - x_i)(z_i - z)}{((x_i - x)^2 + y^2 + (z_i - z)^2)^{\frac{3}{2}}} \qquad (28)$$

These three derivatives are finally evaluated at the stationary phase point:

$$\frac{\partial^2\Phi}{\partial x_i^2}\Big|_{x_s,z_s} = \frac{k^2 - k_{x_i}^2}{y}\,\frac{\sqrt{k^2 - k_{x_i}^2 - k_{z_i}^2}}{k^3} \qquad (29)$$
$$\frac{\partial^2\Phi}{\partial z_i^2}\Big|_{x_s,z_s} = \frac{k^2 - k_{z_i}^2}{y}\,\frac{\sqrt{k^2 - k_{x_i}^2 - k_{z_i}^2}}{k^3} \qquad (30)$$

Finally:

$$\frac{\partial^2\Phi}{\partial x_i \partial z_i}\Big|_{x_s,z_s} = -\frac{(x - x_s)(z_s - z)}{((x_s - x)^2 + y^2 + (z_s - z)^2)^{\frac{3}{2}}} \qquad (31)$$
$$= y^{-1}k^{-3}k_{x_i}k_{z_i}\,(k^2 - k_{x_i}^2 - k_{z_i}^2)^{\frac{1}{2}} \qquad (32)$$

It is then required to evaluate $(\frac{\partial^2\Phi}{\partial x_i \partial z_i}|_{x_s,z_s})^2$:

$$\Big(\frac{\partial^2\Phi}{\partial x_i \partial z_i}\Big|_{x_s,z_s}\Big)^2 = y^{-2}k^{-6}\,k_{x_i}^2 k_{z_i}^2\,(k^2 - k_{x_i}^2 - k_{z_i}^2) \qquad (33)$$

Finally, it is necessary to evaluate the expression of the amplitude term $R(x_s, z_s)$, as well as the expression of the phase term at the stationary point $\Phi(x_s, z_s)$:

$$R(x_s, z_s) = \sqrt{(x_s - x)^2 + y^2 + (z_s - z)^2} \qquad (34)$$
$$= \frac{ky}{\sqrt{k^2 - k_{x_i}^2 - k_{z_i}^2}} \qquad (35)$$

$$\Phi(x_s, z_s) = -\sqrt{(x_s - x)^2 + y^2 + (z_s - z)^2} - \frac{k_{x_i}}{k}x_s - \frac{k_{z_i}}{k}z_s \qquad (36)$$

$$= -\frac{k - (k_{x_i}^2/k) - (k_{z_i}^2/k)}{\sqrt{k^2 - k_{x_i}^2 - k_{z_i}^2}}\, y - \frac{k_{x_i}}{k}x - \frac{k_{z_i}}{k}z \qquad (37)$$

The magnitude and phase term evaluated at the stationary point can then be extracted from the integral:

$$E_i = \frac{e^{jk\Phi(x_s,z_s)}}{R(x_s, z_s)}\, I_g \qquad (38)$$

where I_g is a Gaussian integral evaluated around the stationary phase point [?], [?]:

$$I_g = \int_{x_i}\int_{z_i} \exp\Big(jk\frac{1}{2}\Big[\alpha(x_i - x_s)^2 + \beta(z_i - z_s)^2 + 2\gamma(x_i - x_s)(z_i - z_s)\Big]\Big)\partial x_i\, \partial z_i \qquad (39)$$

with $\alpha = -\frac{\partial^2\Phi}{\partial x_i^2}|_{x_s,z_s}$, $\beta = -\frac{\partial^2\Phi}{\partial z_i^2}|_{x_s,z_s}$ and $\gamma = -\frac{\partial^2\Phi}{\partial x_i \partial z_i}|_{x_s,z_s}$.

Having $\alpha\beta > \gamma^2$ and $\alpha < 0$, Eq. (38) then takes the following form:

$$E_i = -\frac{j2\pi}{k}\, R(x_s, z_s)^{-1} e^{jk\Phi(x_s,y_s)} \left(\left|\frac{\partial^2\Phi}{\partial x_i^2}\Big|_{x_s,z_s}\frac{\partial^2\Phi}{\partial z_i^2}\Big|_{x_s,z_s} - \Big(\frac{\partial^2\Phi}{\partial x_i \partial z_i}\Big|_{x_s,z_s}\Big)^2\right|\right)^{-\frac{1}{2}} \qquad (40)$$

$$= -\frac{j2\pi}{k}\,\frac{\sqrt{k^2 - k_{x_i}^2 - k_{z_i}^2}}{ky}\,\frac{k^2 y}{k^2 - k_{x_i}^2 - k_{z_i}^2}\, \exp\left(-j\left(\frac{k^2 - k_{x_i}^2 - k_{z_i}^2}{\sqrt{k^2 - k_{x_i}^2 - k_{z_i}^2}}\, y + k_{x_i}x + k_{z_i}z\right)\right) \qquad (41)$$

$$= \frac{-j2\pi}{\sqrt{k^2 - k_{x_i}^2 - k_{z_i}^2}}\, \exp(-j\sqrt{k^2 - k_{x_i}^2 - k_{z_i}^2}\, y)\, \exp(-jk_{x_i}x)\exp(-jk_{z_i}z) \qquad (42)$$

Finally, we recall the initial expression of the MIMO signal $S(k_{x_t}, k_{z_t}, k_{x_r}, k_{z_r}, k)$ expressed in the k-space, as well as its equivalent expression obtained by applying the stationary phase method:

$$S = \int_r \frac{\sigma(r)}{16\pi^2}\Big(\int_{A_t}\frac{e^{-jkR_t}}{R_t}e^{jk_{x_t}x_t}e^{jk_{z_t}z_t}\, dA_t\Big)\Big(\int_{A_r}\frac{e^{-jkR_r}}{R_r}e^{jk_{x_r}x_r}e^{jk_{z_r}z_r}\, dA_r\Big)\, d^3r \qquad (43)$$

$$= \frac{4\pi^2}{16\pi^2 k_{y_t}k_{y_r}}\int_r \sigma(r)\, e^{-jk_{y_t}y}\, e^{-jk_{x_t}x}\, e^{-jk_{z_t}z}\, e^{-jk_{y_r}y}\, e^{-jk_{x_r}x}\, e^{-jk_{z_r}z}\, d^3r \qquad (44)$$

$$= \frac{1}{4k_{y_t}k_{y_r}}\int_r \sigma(r)\, e^{-jk_y y}\, e^{-jk_x x}\, e^{-jk_z z}\, d^3r \qquad (45)$$

where the association of transverse components corresponding to the plane waves emitted and received give rise to new projections of composite wave vectors interrogating the target space:

$$k_{y_t} = \sqrt{k^2 - k_{x_t}^2 - k_{z_t}^2} \qquad (46)$$
$$k_{y_r} = \sqrt{k^2 - k_{x_r}^2 - k_{z_r}^2} \qquad (47)$$
$$k_x = k_{x_t} + k_{x_r} \qquad (48)$$
$$k_y = k_{y_t} + k_{y_r} \qquad (49)$$
$$k_z = k_{z_t} + k_{z_r} \qquad (50)$$

Fromenteze, T., Yurduseven, O., Berland, F., Decroze, C., Smith, D. R., & Yarovoy, A. G. (2019). A Transverse Spectrum Deconvolution Technique for MIMO Short-Range Fourier Imaging. *IEEE Transactions on Geoscience and Remote Sensing*.

Improving the MIMO RMA

Introducing the transverse spectrum deconvolution (TSD RMA)

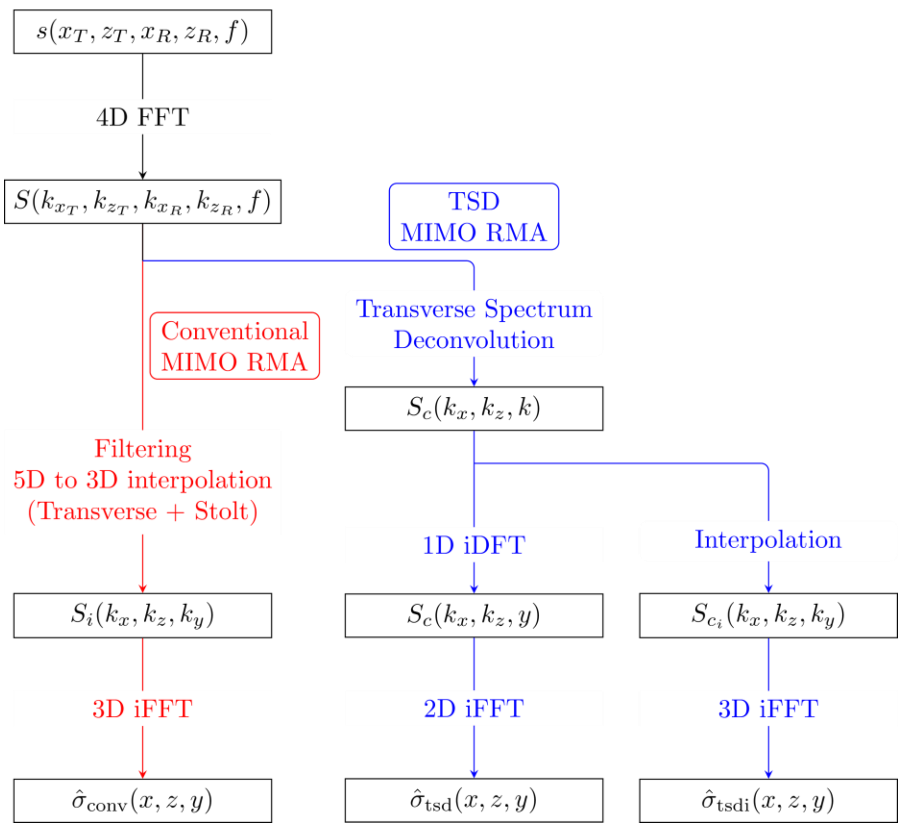

Core idea: it's all about radiation patterns

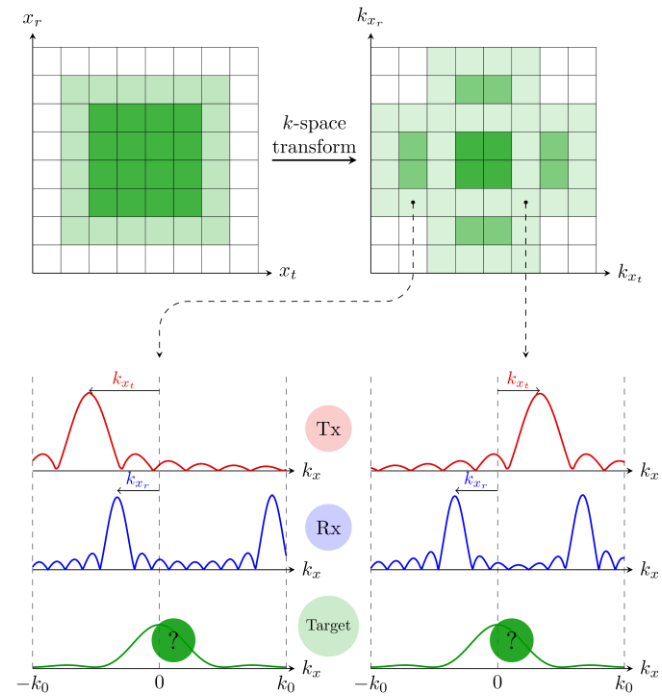

Main advantages:
- more intuitive and visual approach
- k-space patterns depend only on the spatial sampling not on the frequency

Fromenteze, T., Yurduseven, O., Berland, F., Decroze, C., Smith, D. R., & Yarovoy, A. G. (2019). A Transverse Spectrum Deconvolution Technique for MIMO Short-Range Fourier Imaging. *IEEE Transactions on Geoscience and Remote Sensing*.

Improving the MIMO RMA

Core idea: it's all about radiation patterns

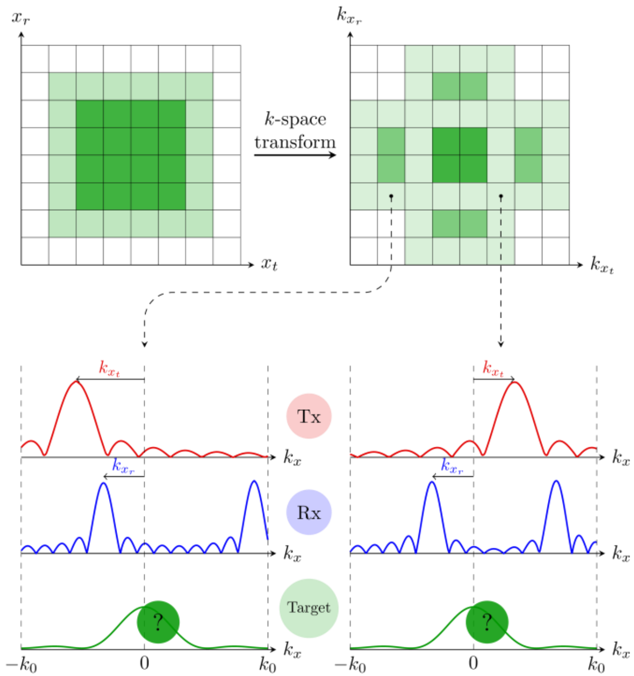

Main advantages:
- more intuitive and visual approach
- k-space patterns depend only on the spatial sampling **not on the frequency**

Interrogation of a spectrum through known radiation patterns

Target spectrum

$$S = \int_{k_x} \int_{k_z} P_t(k_x - k_{x_t}, k_z - k_{z_t}) \, S_c(k_x, k_z, k) P_r(k_x - k_{x_r}, k_z - k_{z_r}) \, dk_x \, dk_z$$

Tx radiation patterns

Rx radiation patterns

Expression in matrix form and separation of spatial variables

$$S(k) = P_x \; S_c(k) \; P_z$$

Reconstruction of transverse spectral data by pseudo-inversion

$$\hat{S}_c(k) = P_x^+ \; S(k) \; P_z^+$$

1. Interpolation calculations are replaced by matrix multiplication
2. These calculations are made without any frequency dependence
3. RAM consumption is greatly reduced
4. Reconstructions are more accurate

Fromenteze, T., Yurduseven, O., Berland, F., Decroze, C., Smith, D. R., & Yarovoy, A. G. (2019). A Transverse Spectrum Deconvolution Technique for MIMO Short-Range Fourier Imaging. *IEEE Transactions on Geoscience and Remote Sensing*.

Improving the MIMO RMA

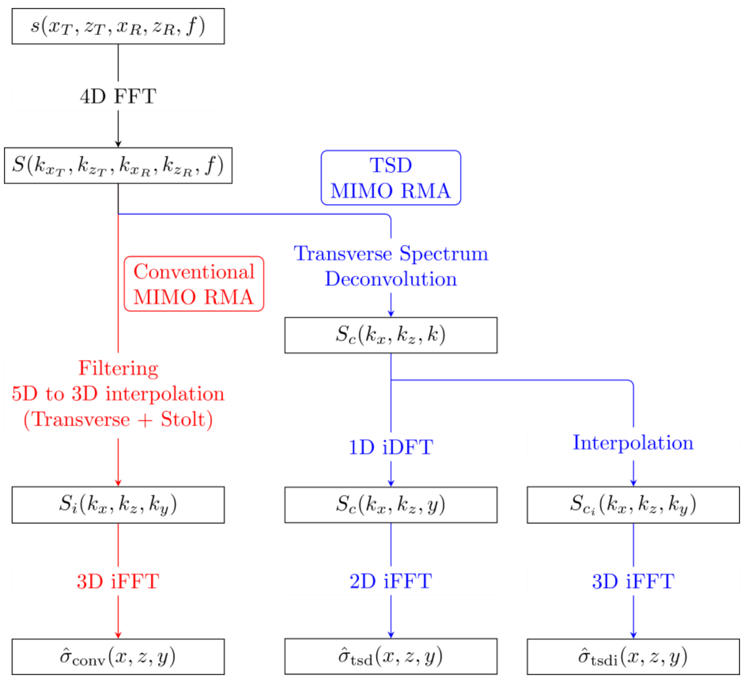

Definition of a new state of the art of range-migration algorithms

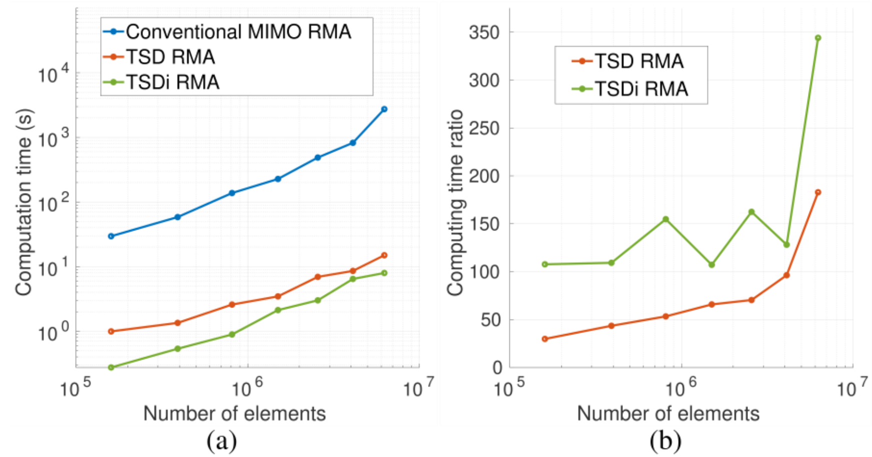

Application to large and densely populated MIMO arrays

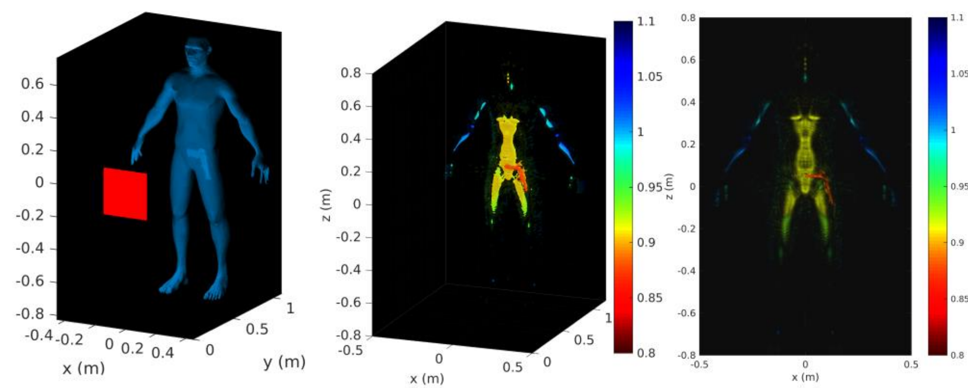

Validation with a MIMO array of 71^4 radiating elements
more than 25 million interactions at each frequency

Fromenteze, T., Yurduseven, O., Berland, F., Decroze, C., Smith, D. R., & Yarovoy, A. G. (2019). A Transverse Spectrum Deconvolution Technique for MIMO Short-Range Fourier Imaging. *IEEE Transactions on Geoscience and Remote Sensing*.

Polarimetric computational imaging

Motivation: Study of anisotropic/multiple-bounce scattering

Far-field: Estimation of soil parameters

(a) Original Image

(a) Classification Map

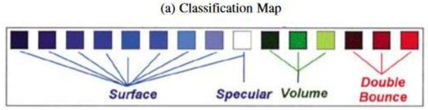

Unsupervised Terrain Classification Preserving Polarimetric Scattering Characteristics"
J-S Lee, M.R. Grunes, E. Pottier, L. Ferro-Famil - IEEE TGRS, 2004

Short-range: Threat detection

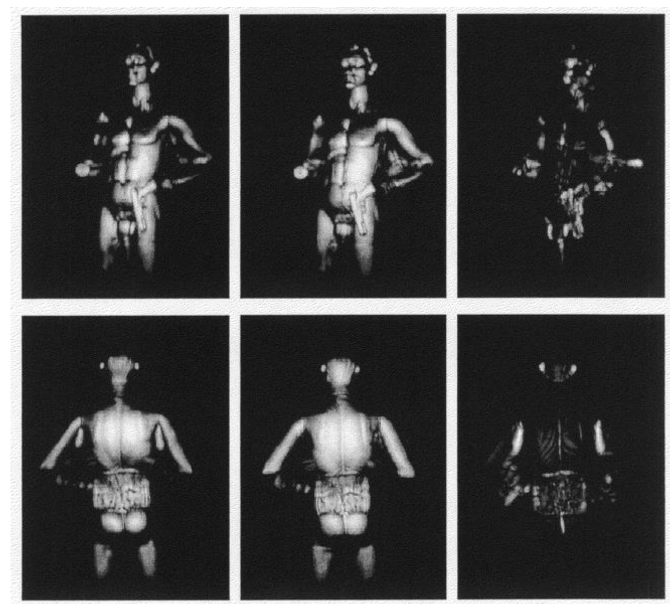

Holographic arrays for multi-path imaging artifact reduction"
D.L. McMakin, D.M. Sheen, T.E. Hall - US Patent, 2005

Polarimetric computational localization

Conventional approach

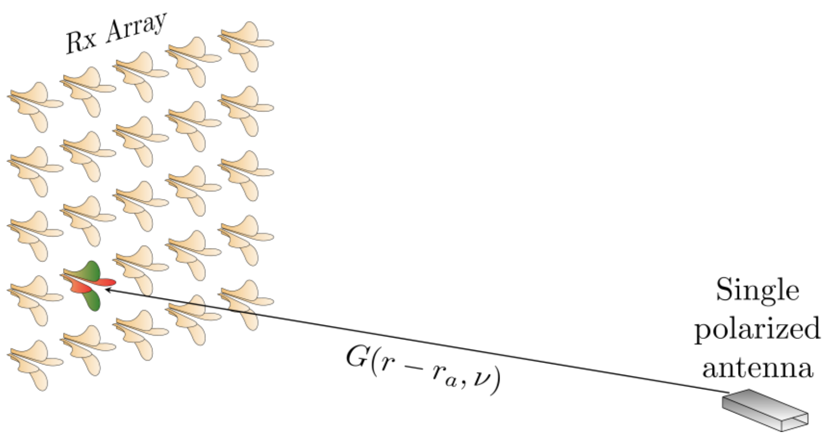

Computational approach

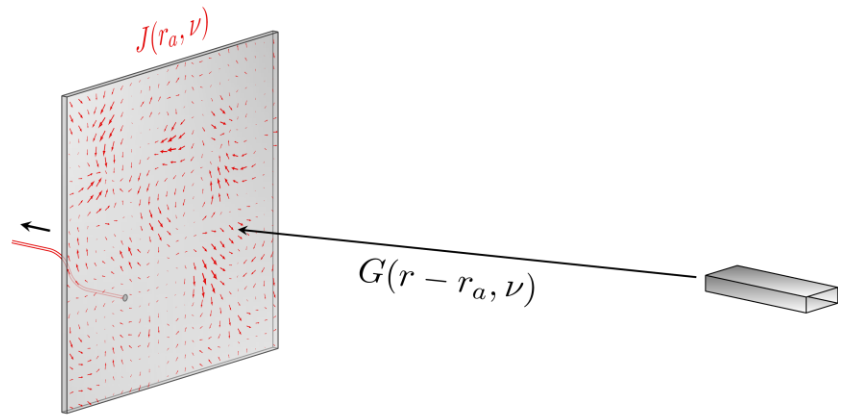

Doubles the hardware constraints compared to scalar systems

Fromenteze, T., Boyarsky, M., Yurduseven, O., Gollub, J., Marks, D. L., & Smith, D. R. (2017, July). Computational polarimetric localization with a radiating metasurface. In *2017 IEEE International Symposium on Antennas and Propagation & USNC/URSI National Radio Science Meeting* (pp. 407-408). IEEE.

Polarimetric computational localization

We now get out of the scalar approximation

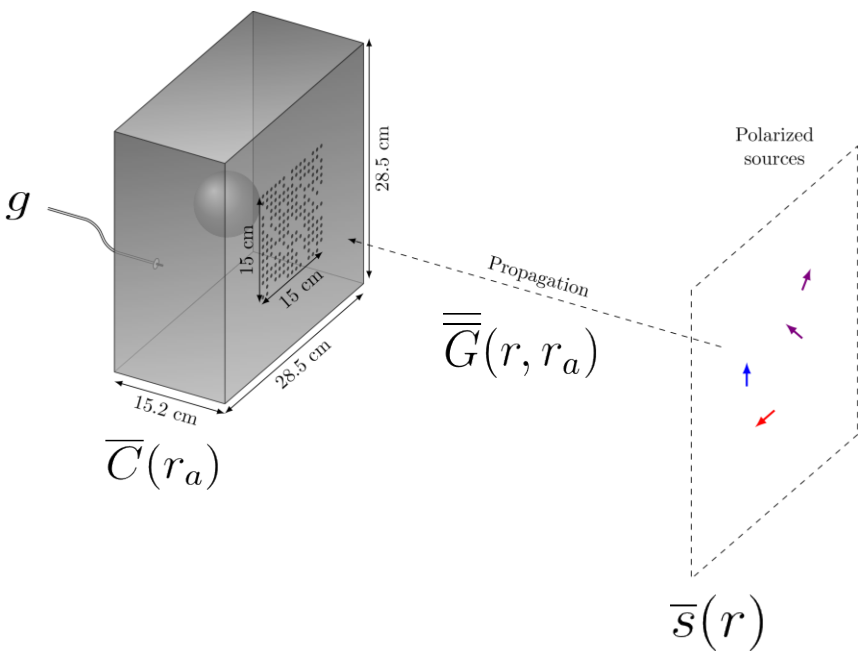

To lighten the notation, frequencies are implicit

Measured signal

$$g = \int_{r_a} \int_{r} \overline{C}(r_a) \overline{\overline{G}}(r, r_a) \overline{s}(r) dr_a dr$$

in the polarization space:

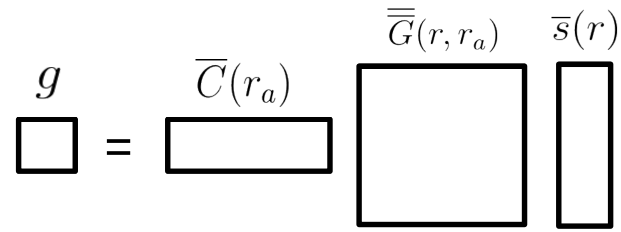

$\overline{s}(r)$ Polarized sources

$\overline{C}(r_a)$ Transfer function of the cavity (3 polarizations on its surface)

$\overline{\overline{G}}(r, r_a)$ Dyadic Green's function

$$\overline{\overline{G}}(r, r_a) = (1 + \frac{1}{k^2} \Delta\Delta \cdot) \frac{\exp(-jk|r - r_a|)}{|r - r_a|} \overline{\overline{I}}$$

Fromenteze, T., Boyarsky, M., Yurduseven, O., Gollub, J., Marks, D. L., & Smith, D. R. (2017, July). Computational polarimetric localization with a radiating metasurface. In *2017 IEEE International Symposium on Antennas and Propagation & USNC/URSI National Radio Science Meeting* (pp. 407-408). IEEE.

Polarimetric computational localization

We now get out of the scalar approximation

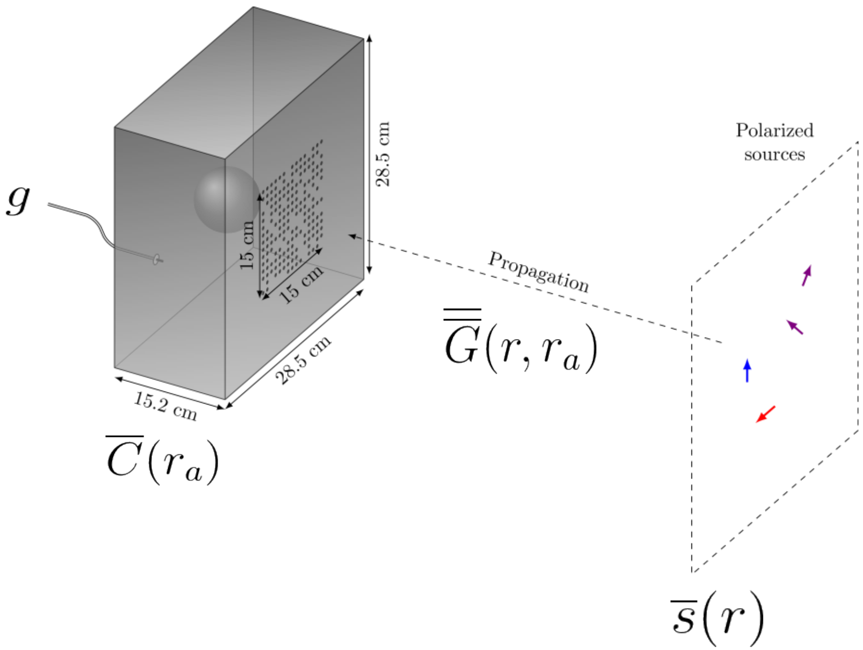

Measured signal

$$g = \int_{r_a} \int_r \overline{C}(r_a)\overline{\overline{G}}(r, r_a)\overline{s}(r)dr_a dr$$

Discrete model

$$g = \overline{C}\,\overline{\overline{G}}\overline{s}$$

Reconstruction

$$\hat{\overline{s}} = \left(\overline{\overline{G}}\,\overline{C}\right)^{+} g$$

To lighten the notation, frequencies are implicit

Fromenteze, T., Boyarsky, M., Yurduseven, O., Gollub, J., Marks, D. L., & Smith, D. R. (2017, July). Computational polarimetric localization with a radiating metasurface. In *2017 IEEE International Symposium on Antennas and Propagation & USNC/URSI National Radio Science Meeting* (pp. 407-408). IEEE.

Polarimetric computational localization

Near field scans $\overline{C}(r_a)$

Cavity quality factor
Q~12 000

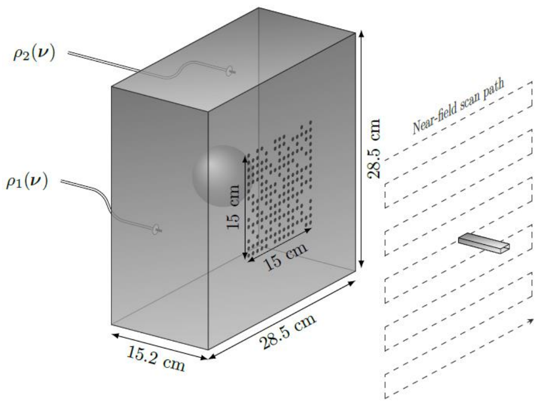

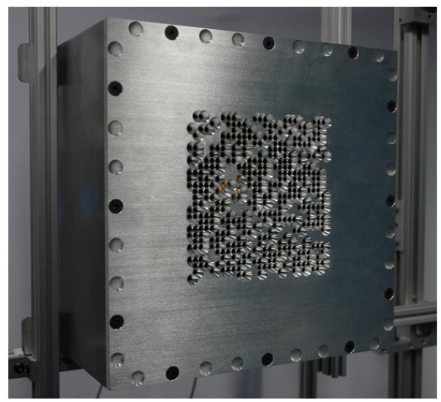

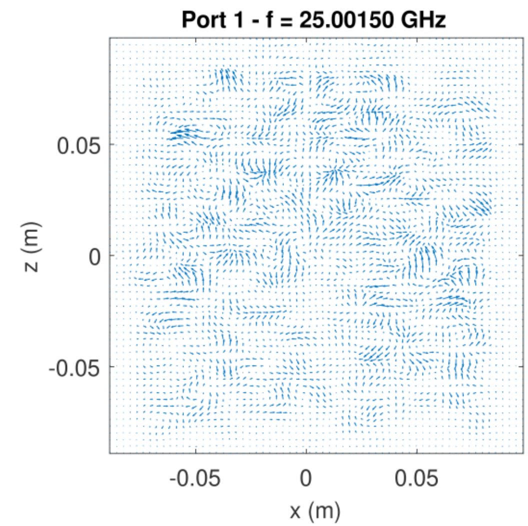

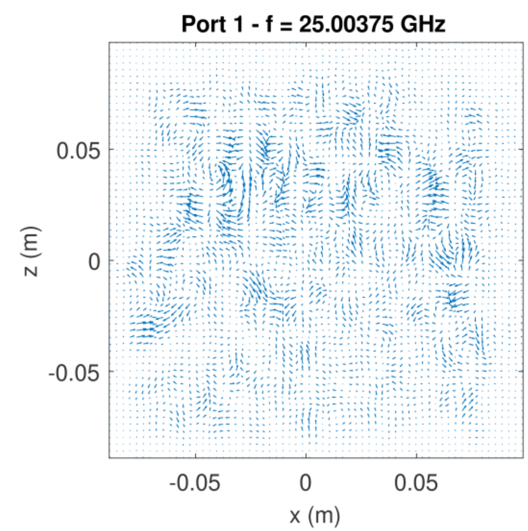

Fromenteze, T., Boyarsky, M., Yurduseven, O., Gollub, J., Marks, D. L., & Smith, D. R. (2017, July). Computational polarimetric localization with a radiating metasurface. In *2017 IEEE International Symposium on Antennas and Propagation & USNC/URSI National Radio Science Meeting* (pp. 407-408). IEEE.

Polarimetric computational imaging

Near field scans $\overline{C}(r_a)$

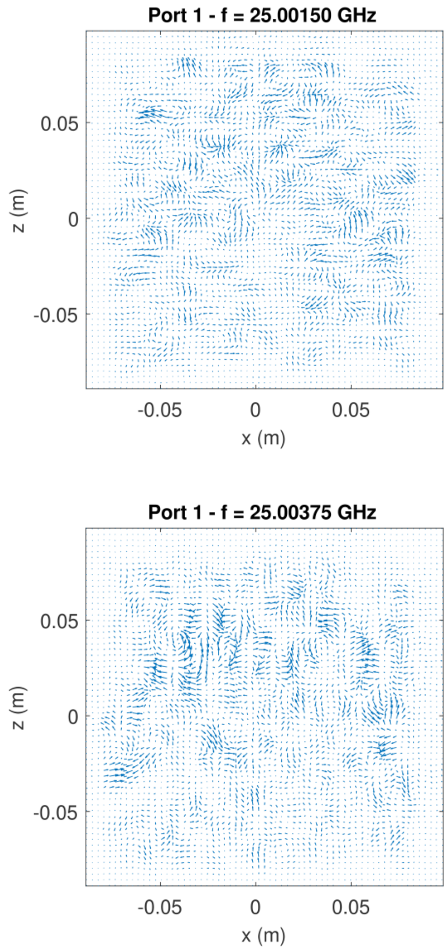

Spatial correlations:

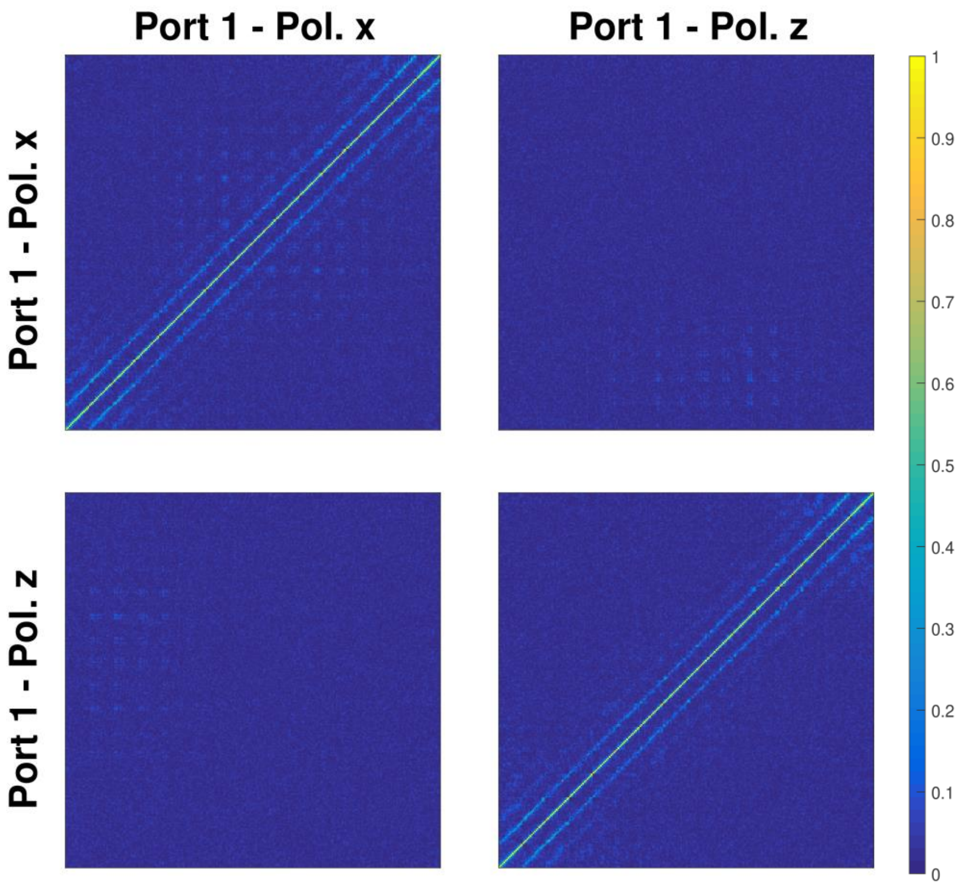

Fromenteze, T., Boyarsky, M., Yurduseven, O., Gollub, J., Marks, D. L., & Smith, D. R. (2017, July). Computational polarimetric localization with a radiating metasurface. In *2017 IEEE International Symposium on Antennas and Propagation & USNC/URSI National Radio Science Meeting* (pp. 407-408). IEEE.

Polarimetric computational localization

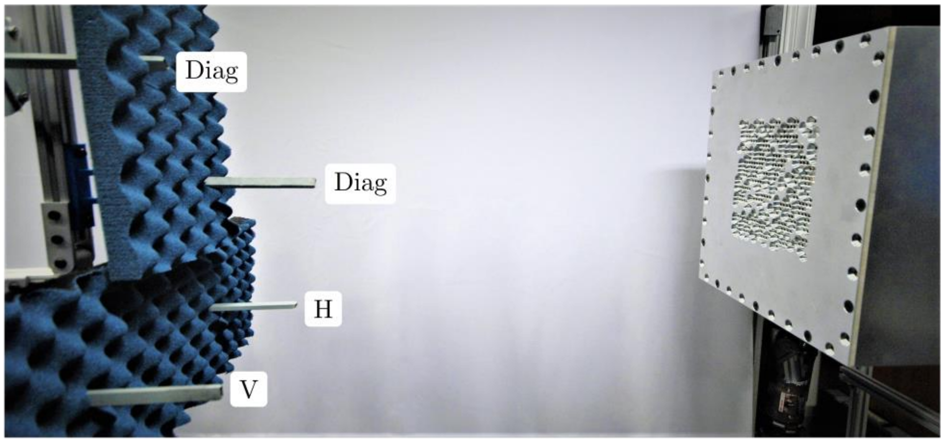

Reconstruction

$$\hat{s} = \left(\overline{\overline{G}}\,\overline{C}\right)^{+} g$$

- Frequency range : 18.5-26 GHz
- 801 Frequency samples
- 134 × 36 × 134 ~ 650 000 voxels
- Volume of 0.8 × 0.75 × 0.8 m³
- **Computed in less than a second** using Fourier processing

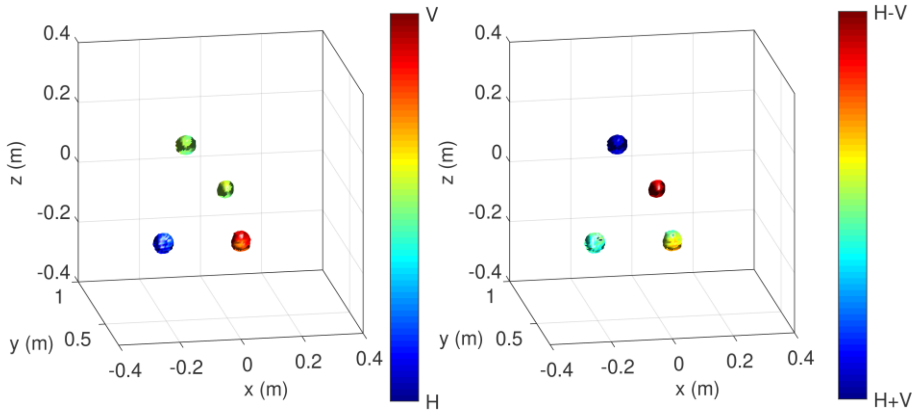

-5dB isosurfaces

Fromenteze, T., Boyarsky, M., Yurduseven, O., Gollub, J., Marks, D. L., & Smith, D. R. (2017, July). Computational polarimetric localization with a radiating metasurface. In *2017 IEEE International Symposium on Antennas and Propagation & USNC/URSI National Radio Science Meeting* (pp. 407-408). IEEE.

Polarimetric computational imaging

Scalar imaging forward model

$$g_{i,j}(\omega) \propto \int_r [E_i . E_j](r,\omega) f(r)\, d^3 r$$

$g_{i,j}(\omega)$ measured frequency-domain signal

$E_i(r,\omega)$ scalar Tx electric field

$E_j(r,\omega)$ scalar Rx electric field

$f(r)$ scalar reflectivity function (Δε(r))

If our target exhibits anisotropic/depolarizing behavior:

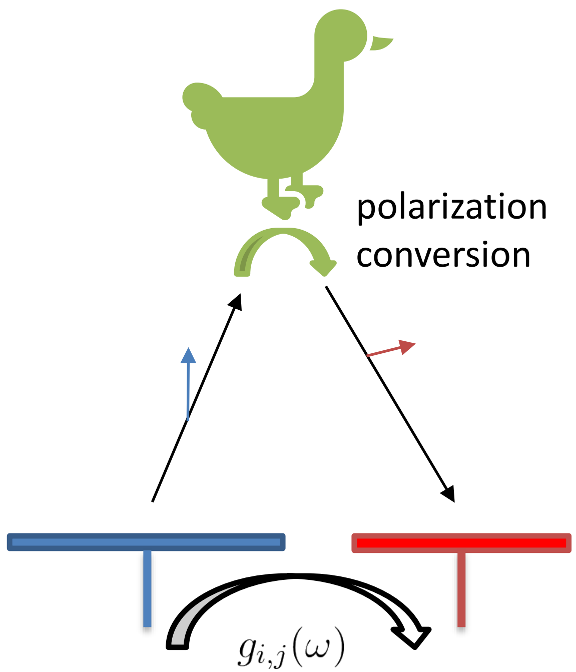

Each point in space must be defined as a susceptibility tensor

$$\overline{\overline{\chi}} = \begin{bmatrix} \chi_{xx} & \chi_{xy} & \chi_{xz} \\ \chi_{yx} & \chi_{yy} & \chi_{yz} \\ \chi_{zx} & \chi_{zy} & \chi_{zz} \end{bmatrix}$$

$$\overline{E_i}^{sca}(r) = \overline{E_i}(r)\overline{\overline{\chi}}(r)$$

The scattered field then interacts with the Rx aperture

$$g_{i,j}(\omega) = \int_r \overline{E_i}(r)\overline{\overline{\chi}}(r)\, \overline{E_j}(r)^T\, dr$$

Fromenteze, T., Yurduseven, O., Boyarsky, M., Gollub, J., Marks, D. L., & Smith, D. R. (2017). Computational polarimetric microwave imaging. *Optics express*, *25*(22), 27488-27505.

Polarimetric computational imaging

Forward model of the polarimetric imaging problem

$$g_{i,j}(\omega) = \int_r \overline{E_i}(r)\,\overline{\overline{\chi}}(r)\,\overline{E_j}(r)^T \, dr$$

Operating with two panels

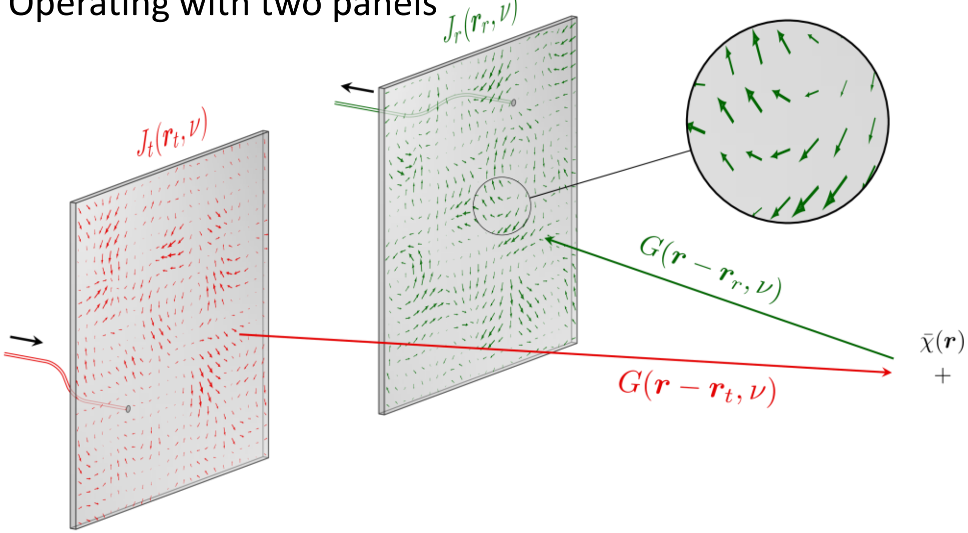

Operating with a single two-ports panel

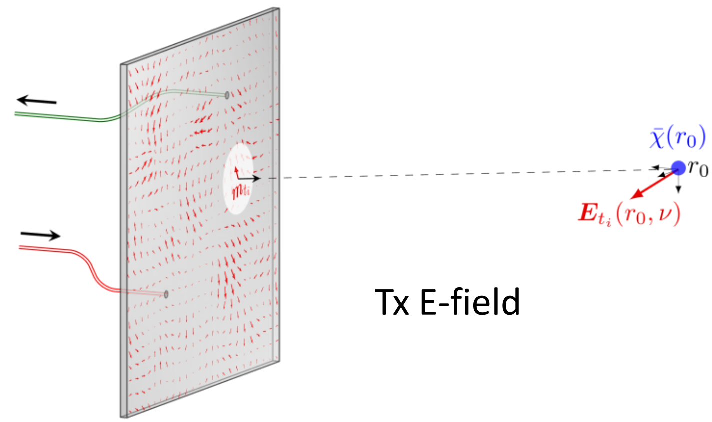

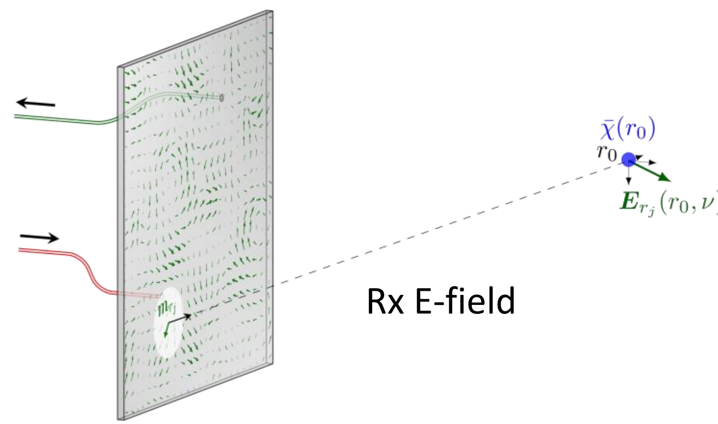

Fromenteze, T., Yurduseven, O., Boyarsky, M., Gollub, J., Marks, D. L., & Smith, D. R. (2017). Computational polarimetric microwave imaging. *Optics express*, *25*(22), 27488-27505.

Polarimetric computational imaging

Forward model of the polarimetric imaging problem

$$g_{i,j}(\omega) = \int_r \overline{E_i}(r)\overline{\overline{\chi}}(r)\,\overline{E_j}(r)^T\,dr$$

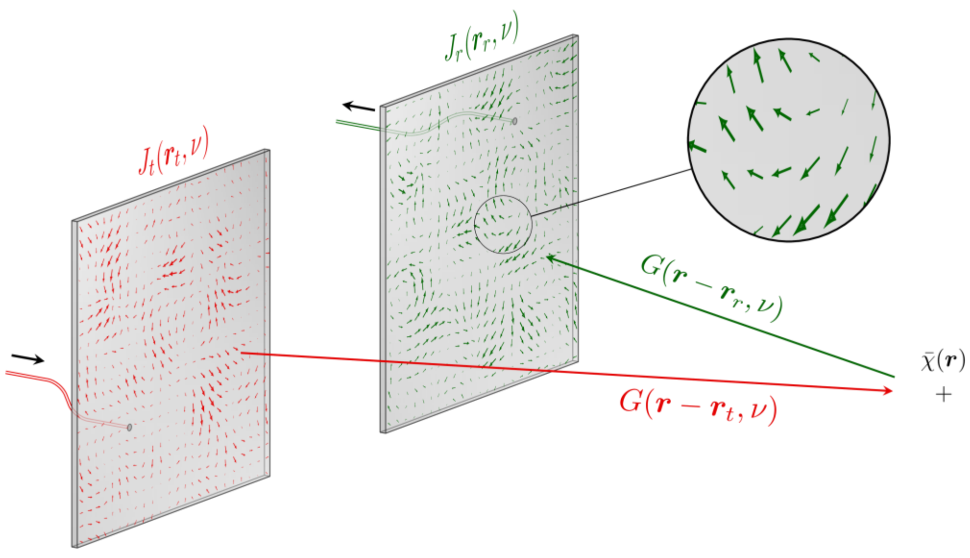

Understanding the physics behind the susceptibility tensors:
The electrons within the target medium are represented by a simple mechanical model

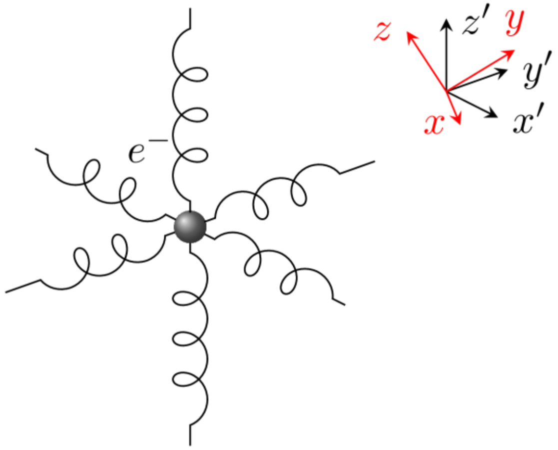

$$\overline{\overline{\chi}}(r) = \overline{\overline{R}}(r)\mathrm{diag}(\bar{\xi}(r))\overline{\overline{R}}(r)^T$$

$\overline{\overline{R}}(r)$ Rotation matrix

$\bar{\xi}(r)$ Diagonalized tensor

Fromenteze, T., Yurduseven, O., Boyarsky, M., Gollub, J., Marks, D. L., & Smith, D. R. (2017). Computational polarimetric microwave imaging. *Optics express*, *25*(22), 27488-27505.

Polarimetric computational imaging

Eigendecompositions helps to identify the directions of the main axis of the tensors (eigenvectors) and the associated eigenvalues define the anisotropic behavior of each voxel

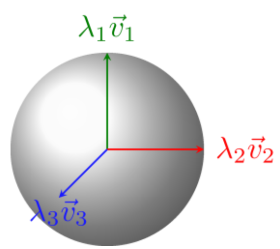

Isotropic scattering

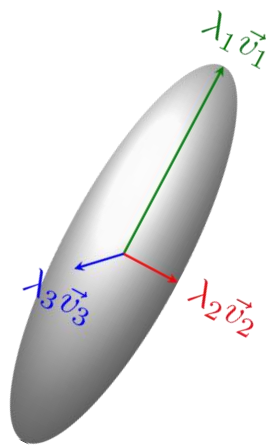

Anisotropic scattering

Understanding the physics behind the susceptibility tensors:
The electrons within the target medium are represented by a simple mechanical model

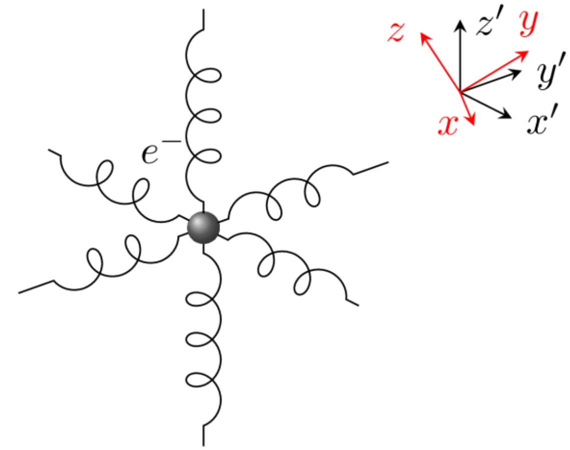

$$\overline{\overline{\chi}}(r) = \overline{\overline{R}}(r)\mathrm{diag}(\bar{\xi}(r))\overline{\overline{R}}(r)^T$$

$\overline{\overline{R}}(r)$ Rotation matrix

$\bar{\xi}(r)$ Diagonalized tensor

Fromenteze, T., Yurduseven, O., Boyarsky, M., Gollub, J., Marks, D. L., & Smith, D. R. (2017). Computational polarimetric microwave imaging. *Optics express*, *25*(22), 27488-27505.

Polarimetric computational imaging

Analogy with **diffusion tensor imaging**
Magnetic Resonance Imaging

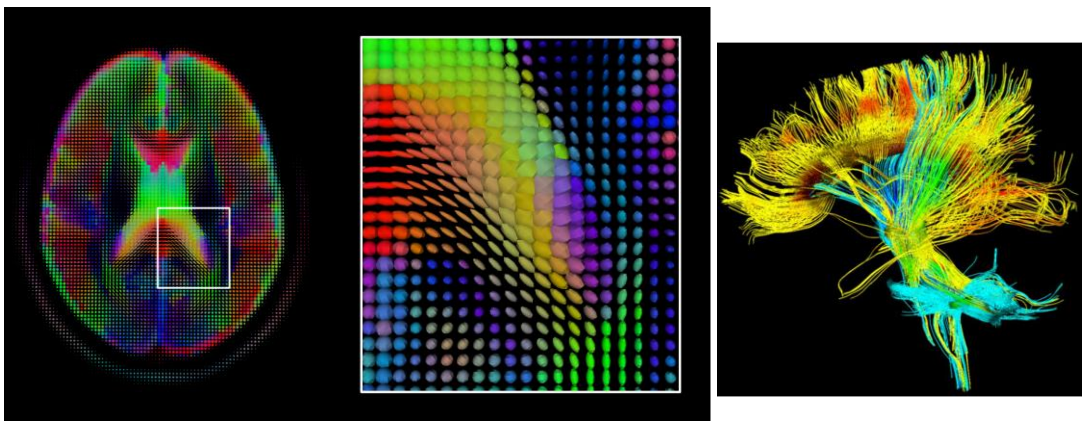

The main axis analysis of the tensors reconstructed in each voxel makes it possible to reconstruct the path of the fibers in the brain

https://en.wikipedia.org/wiki/File:DiffusionMRI_glyphs.png
https://www.siemens-healthineers.com/magnetic-resonance-imaging/options-and-upgrades/clinical-applications/syngo-dti-tractography

Understanding the physics behind the susceptibility tensors:
The electrons within the target medium are represented by a simple mechanical model

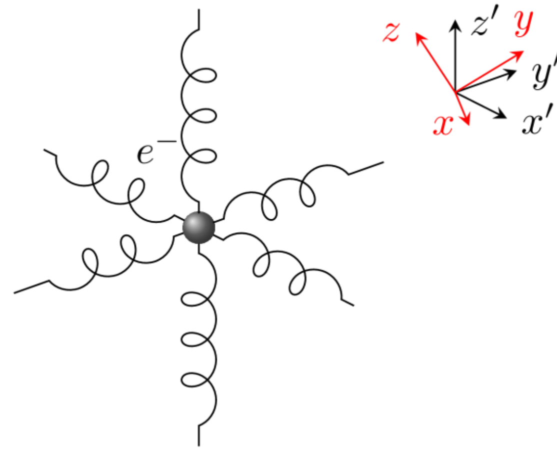

$$\bar{\bar{\chi}}(r) = \bar{\bar{R}}(r)\mathrm{diag}(\bar{\xi}(r))\bar{\bar{R}}(r)^T$$

$\bar{\bar{R}}(r)$ Rotation matrix

$\bar{\xi}(r)$ Diagonalized tensor

Fromenteze, T., Yurduseven, O., Boyarsky, M., Gollub, J., Marks, D. L., & Smith, D. R. (2017). Computational polarimetric microwave imaging. *Optics express*, *25*(22), 27488-27505.

Polarimetric computational imaging

Forward model of the polarimetric imaging problem

$$g_{i,j}(\omega) = \int_r \overline{E_i}(r)\overline{\overline{\chi}}(r)\,\overline{E_j}(r)^T\,dr$$

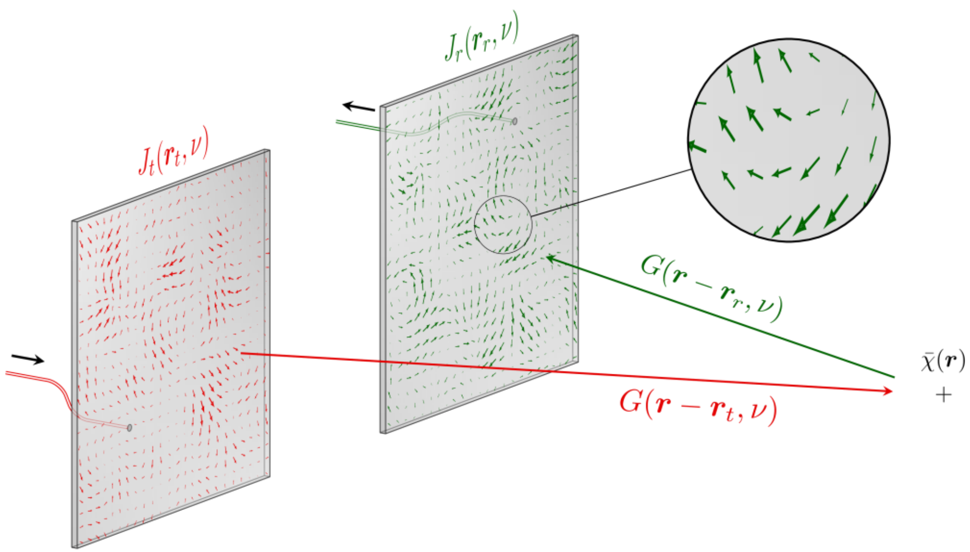

Solving the inverse problem

The Tx and Rx vector fields are inversed to reveal the interaction between each couple of polarization states

$$\hat{\overline{\overline{\chi}}}(r) = \overline{E_i}(r)^+ g_{i,j}\,\overline{E_j}(r)^+$$

Criteria to be met to ensure successful reconstruction

The radiated fields in transmission and reception must be simultaneously orthogonal in three domains:

- in frequency
- in polarization
- spatially

Fromenteze, T., Yurduseven, O., Boyarsky, M., Gollub, J., Marks, D. L., & Smith, D. R. (2017). Computational polarimetric microwave imaging. *Optics express*, *25*(22), 27488-27505.

Polarimetric computational imaging

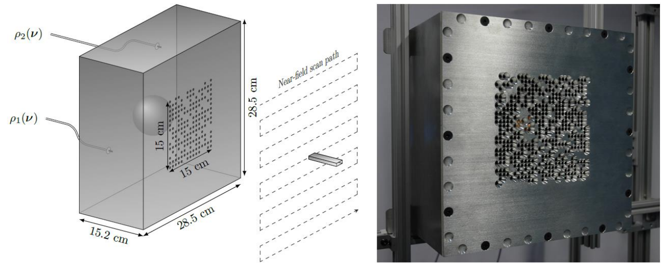

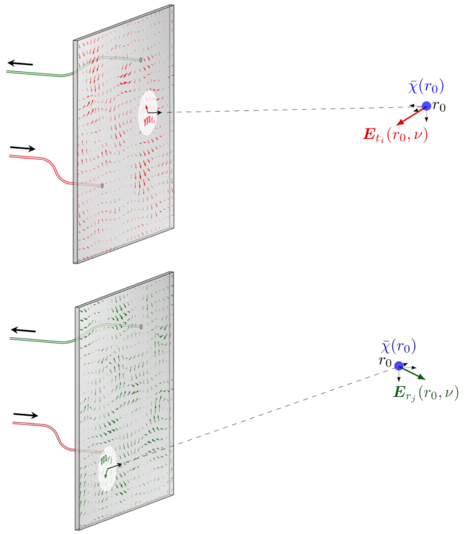

Computing the spatial correlation for each pair of ports and polarizations

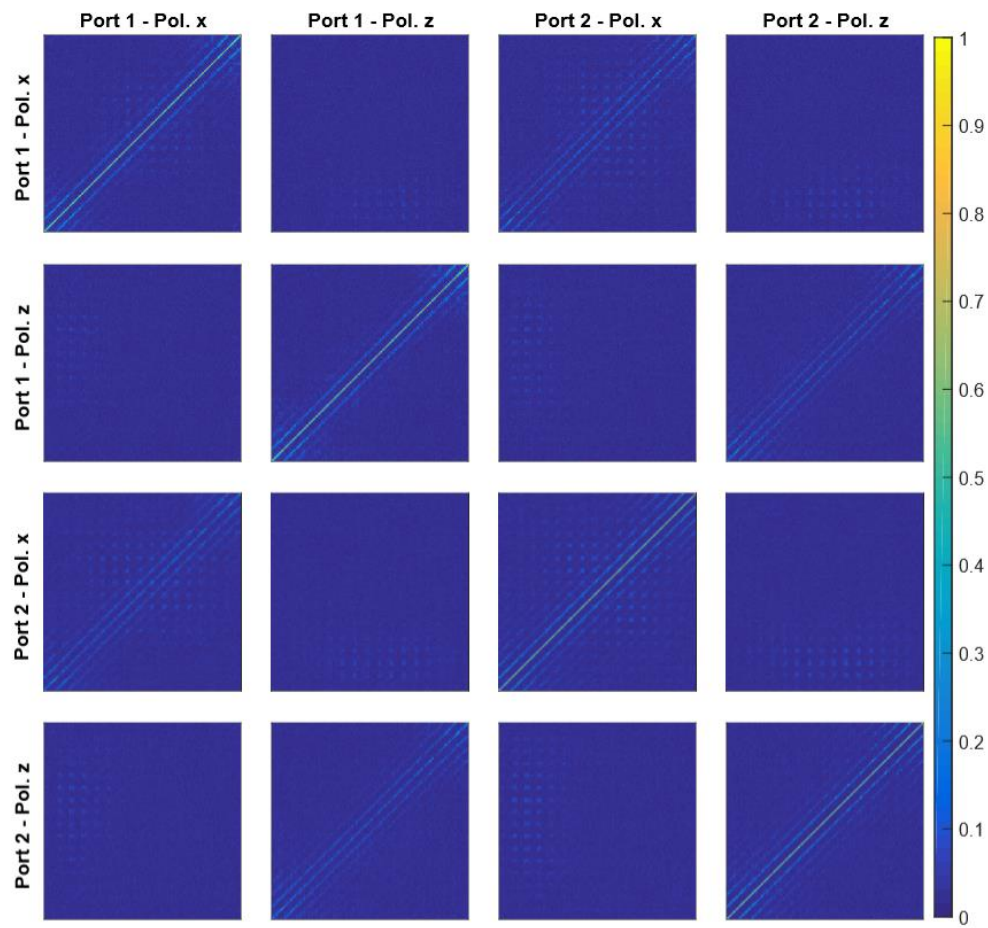

Fromenteze, T., Yurduseven, O., Boyarsky, M., Gollub, J., Marks, D. L., & Smith, D. R. (2017). Computational polarimetric microwave imaging. *Optics express*, *25*(22), 27488-27505.

Polarimetric computational imaging

Experimental validation

Imaging targets made with thin copper wires

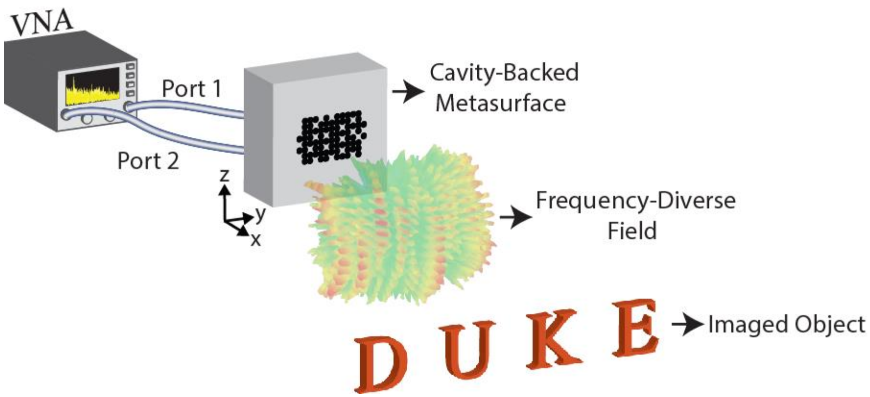

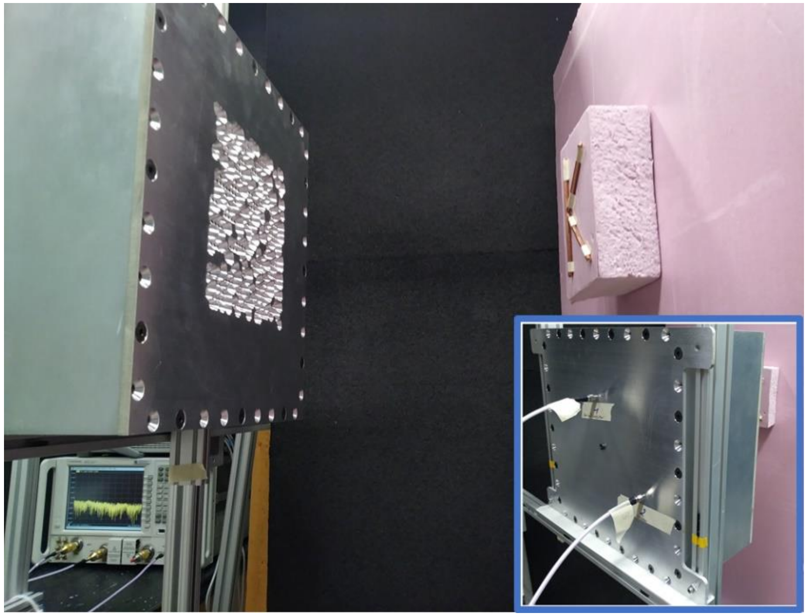

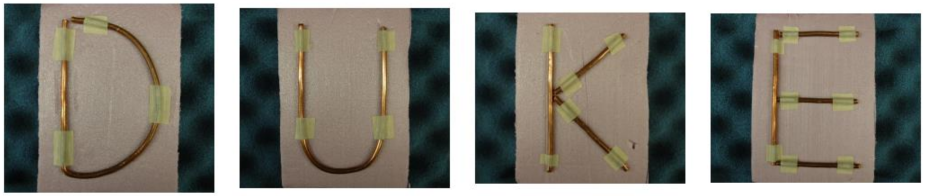

Fig. 10. Copper wire letters used as targets. Each letter is 15×9 cm^2.

Number of frequency samples: 3601

Frequency range: 17.5-26.5 GHz

Fromenteze, T., Yurduseven, O., Boyarsky, M., Gollub, J., Marks, D. L., & Smith, D. R. (2017). Computational polarimetric microwave imaging. *Optics express*, *25*(22), 27488-27505.

Polarimetric computational imaging

Results with the letter D

Reconstructed from the measurement of a single frequency-domain signal

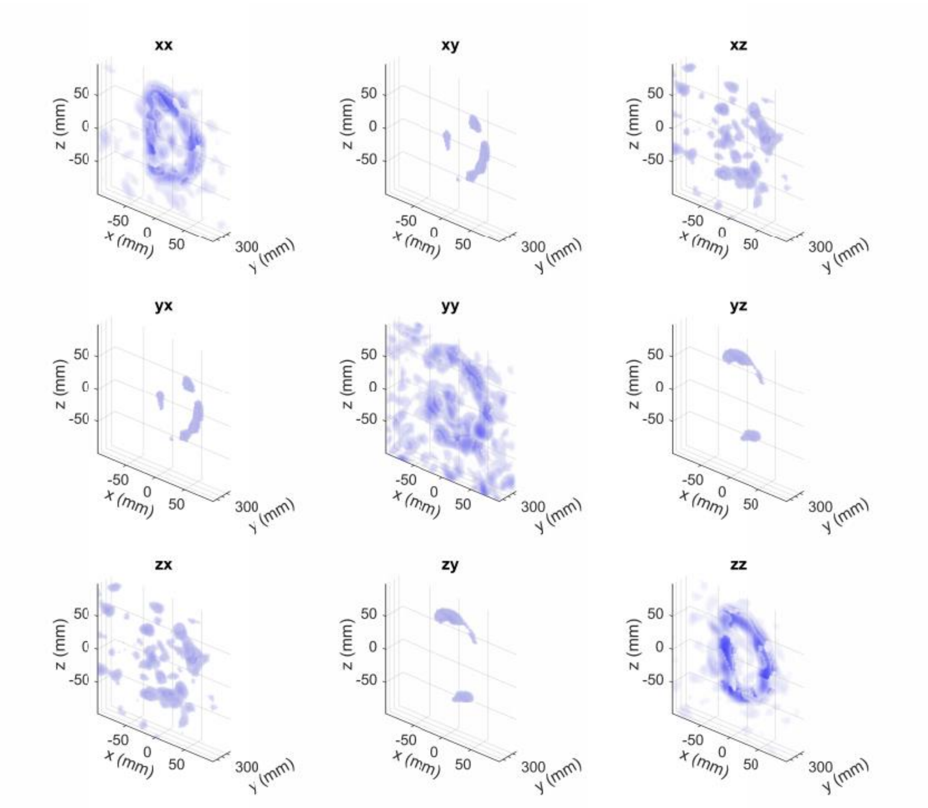

For each voxel

- 9 tensor elements (only 6 are independent)
- each tensor element is a complex value

The diversity of representations of such tensors remains unexplored for these applications

Special feature of the short-range polarimetric imaging

We obtain projections on the propagation axis

x and z are the transverse axis, y is the longitudinal (propagation) axis

Fromenteze, T., Yurduseven, O., Boyarsky, M., Gollub, J., Marks, D. L., & Smith, D. R. (2017). Computational polarimetric microwave imaging. *Optics express*, *25*(22), 27488-27505.

Polarimetric computational imaging

Results with the letter D

Reconstructed from the measurement of a single frequency-domain signal

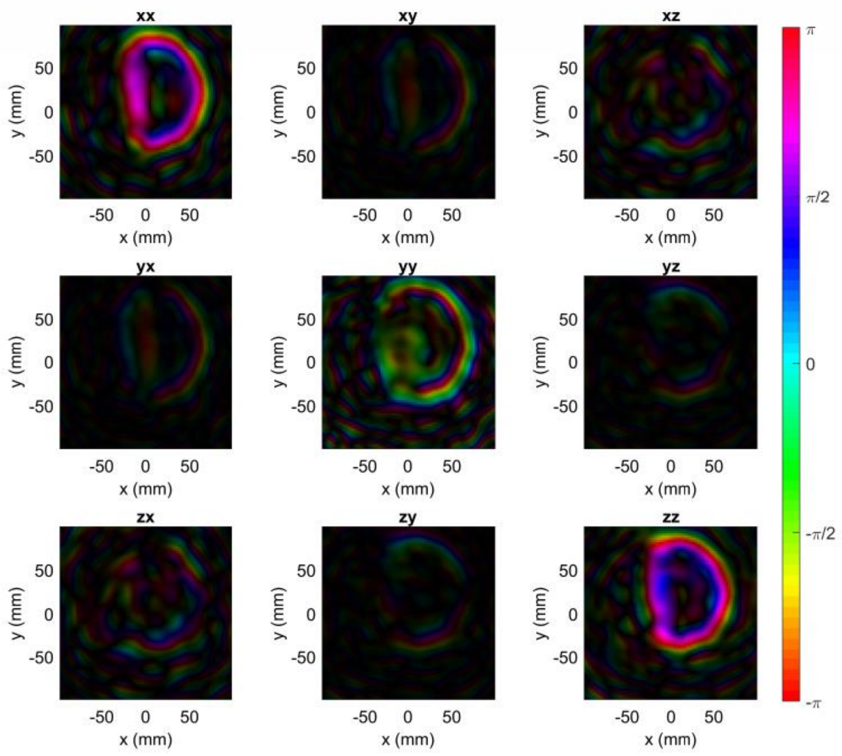

Extraction of a cross-section plan

The phase is included in the reconstructions and can be color-coded to reveal more information

The results are still based Born first approximation we must keep a critical eye on the analysis of the results

x and z are the transverse axis, y is the longitudinal (propagation) axis

Fromenteze, T., Yurduseven, O., Boyarsky, M., Gollub, J., Marks, D. L., & Smith, D. R. (2017). Computational polarimetric microwave imaging. *Optics express*, *25*(22), 27488-27505.

Polarimetric computational imaging

Improvements with basic processing

Correlation of transverse components

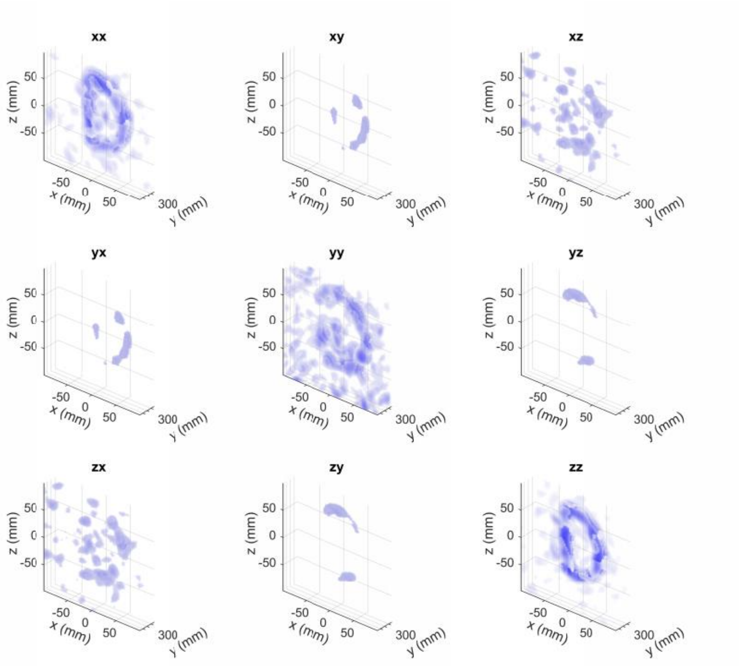

$$\hat{\chi}_{corr}(r) = \hat{\chi}_{x,x}(r) \cdot \hat{\chi}_{z,z}(r)^*$$

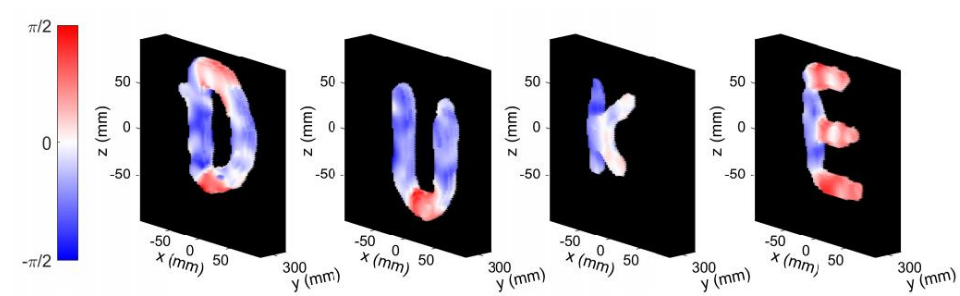

Optimized SNR noise reduced by the coherent sum of the useful parts of the tensor

Anisotropic behavior orientation of copper wires revealed by the phase information

Fromenteze, T., Yurduseven, O., Boyarsky, M., Gollub, J., Marks, D. L., & Smith, D. R. (2017). Computational polarimetric microwave imaging. *Optics express*, *25*(22), 27488-27505.

Polarimetric computational imaging

Going further with eigendecompositions

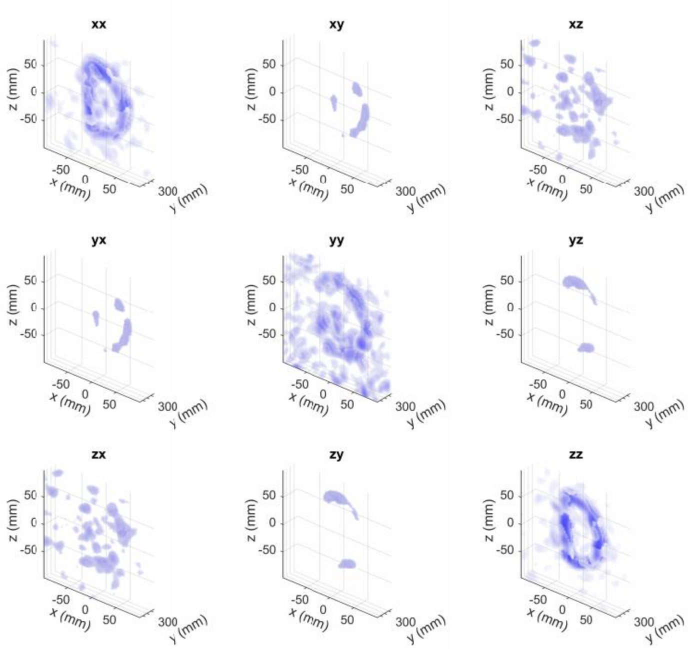

The diagonalization of the tensors is computed for each voxel **on the real and imaginary parts separately**

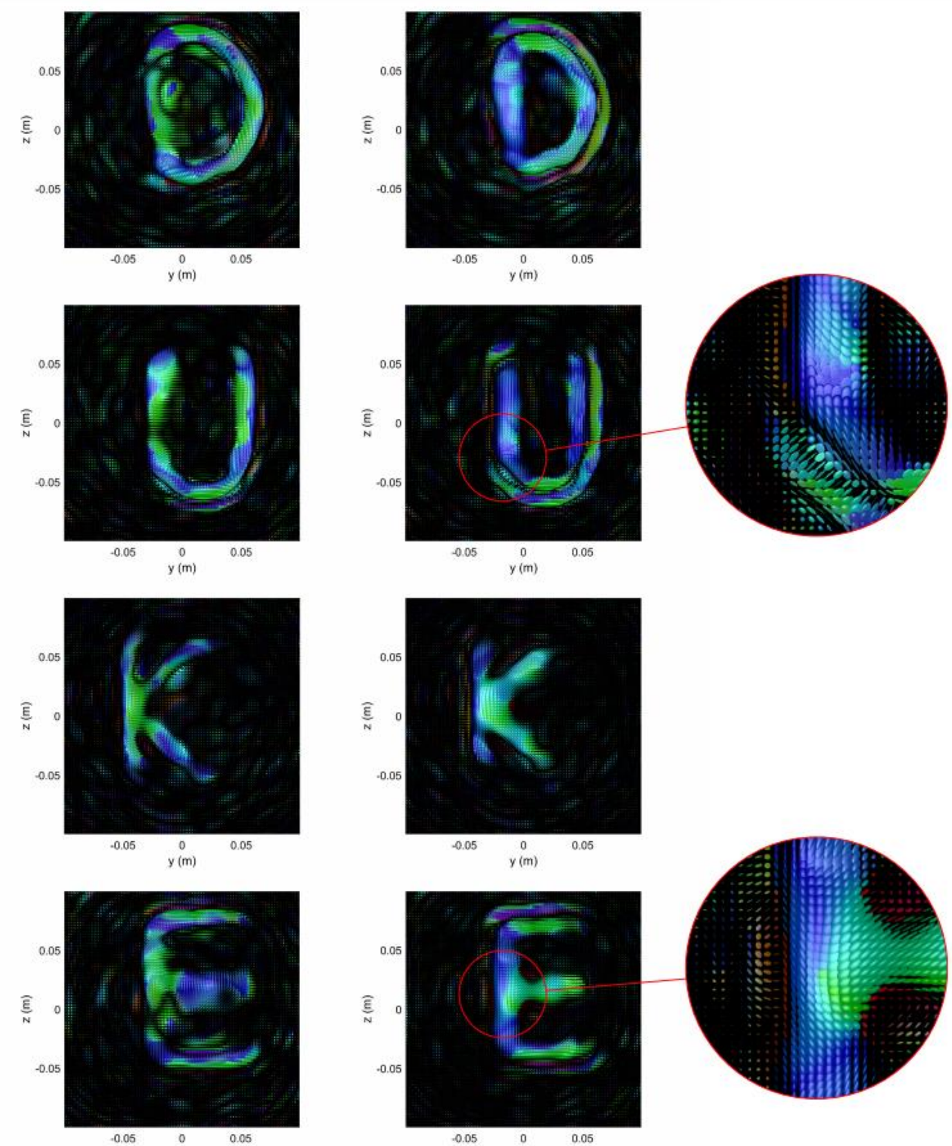

Fromenteze, T., Yurduseven, O., Boyarsky, M., Gollub, J., Marks, D. L., & Smith, D. R. (2017). Computational polarimetric microwave imaging. *Optics express*, *25*(22), 27488-27505.

Polarimetric computational imaging

Going further with eigendecompositions

RGB color-coding according to the orientation of the main axis of each ellipsoid

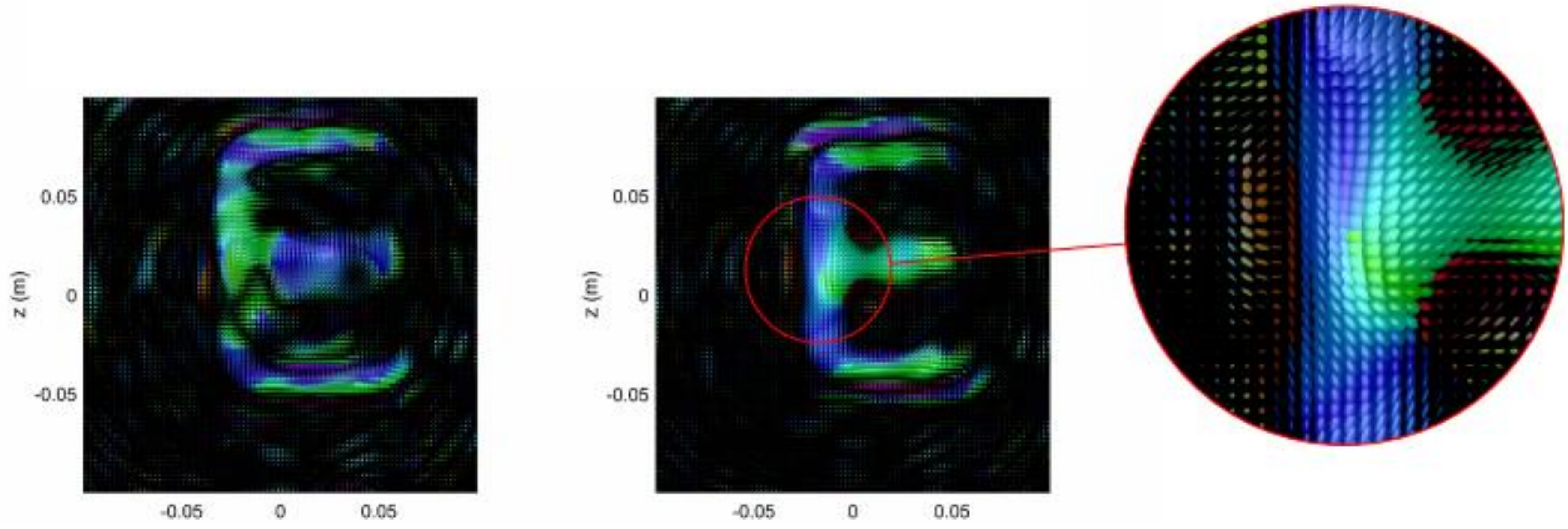

Fromenteze, T., Yurduseven, O., Boyarsky, M., Gollub, J., Marks, D. L., & Smith, D. R. (2017). Computational polarimetric microwave imaging. *Optics express*, *25*(22), 27488-27505.

Polarimetric phaseless imaging

In conclusion of this work

Conventional MIMO polarimetric system

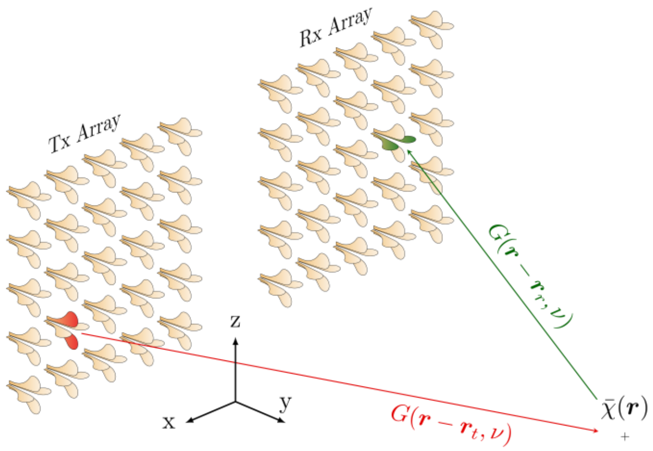

Double the hardware constraints compared to systems based on the scalar approximation

Very few applications in short range imaging due to these limitations

Computational MIMO polarimetric system

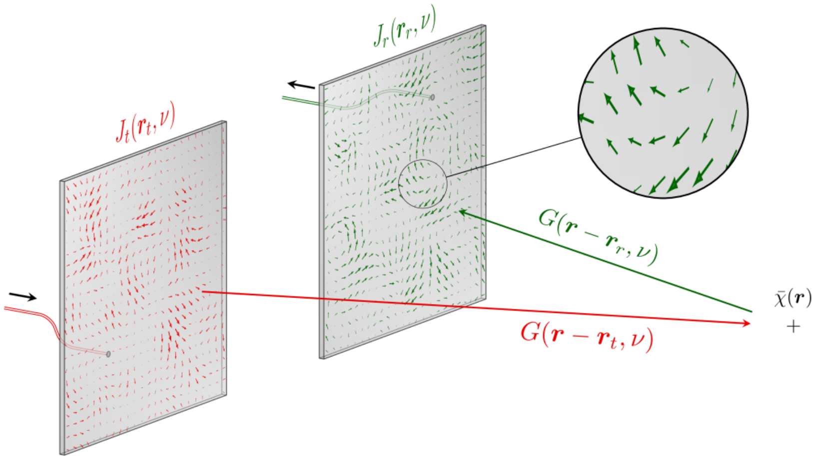

Requires a single measurement chain provided that a full scan of the near fields is carried out

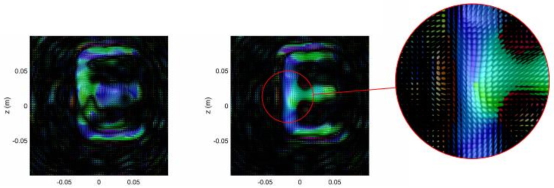

Paves the way for volumetric reconstruction of susceptibility tensors

Fromenteze, T., Yurduseven, O., Boyarsky, M., Gollub, J., Marks, D. L., & Smith, D. R. (2017). Computational polarimetric microwave imaging. *Optics express*, *25*(22), 27488-27505.

Phaseless computational imaging

Conventional MIMO system

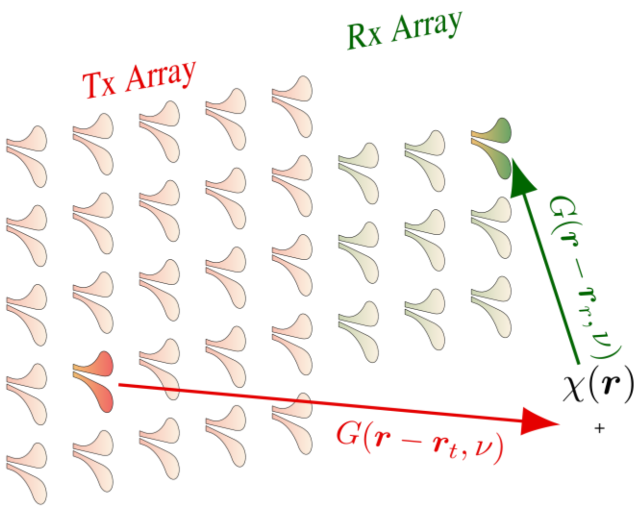

Phase measurement also creates heavy hardware constraints on each measurement chain

Motivation for this work

is it possible to reconstruct images from the intensity measurement of signals that interacted with a target?

In other words, can we replace our VNAs with spectrum analyzers and a little mathematics?

Are computational systems compatible with/supportive of these objectives?

Phaseless computational imaging

First concern: phase information is crucial

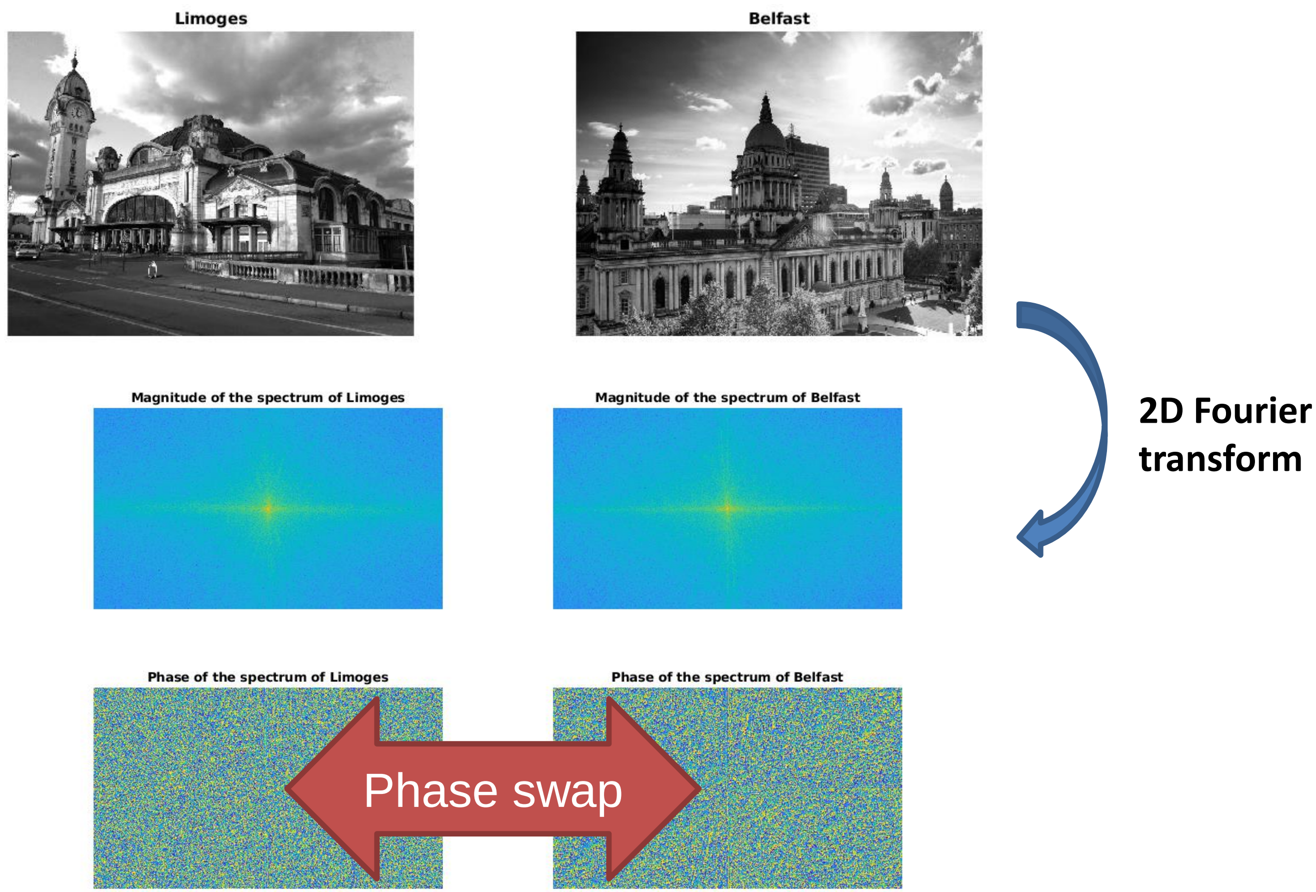

Phaseless computational imaging

First concern: phase information is crucial

Limoges

Belfast

After the phase swap and an inverse 2D Fourier transform

Limoges

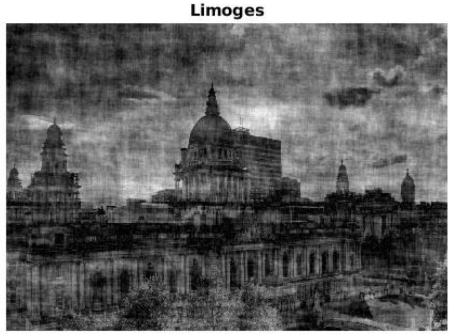

Belfast

Phaseless computational imaging

Key element: phase information can however be encoded in the intensity information

Signals received in an aperture in the presence of two isotropic point sources

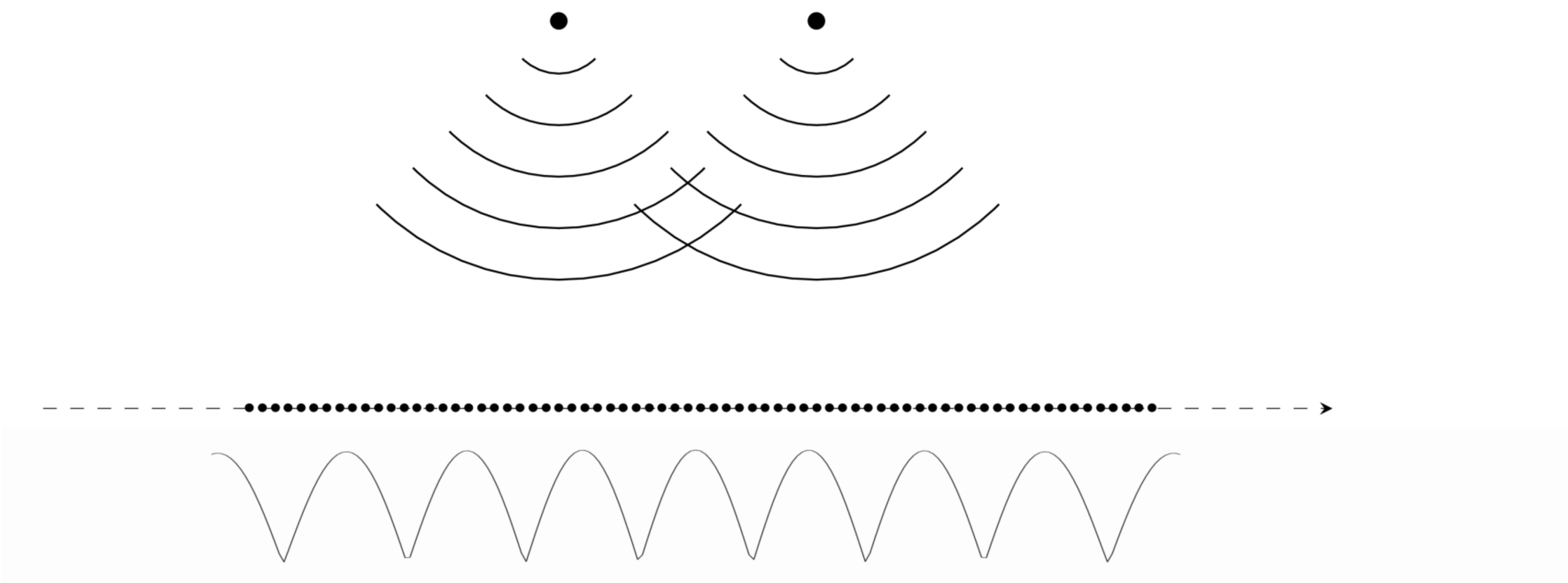

Interferences of complex contributions:
Transformation of phase information into intensity fluctuation
Inverse problem solving: Phase retrieval algorithms

Phaseless computational imaging

Objective: Application to microwave imaging

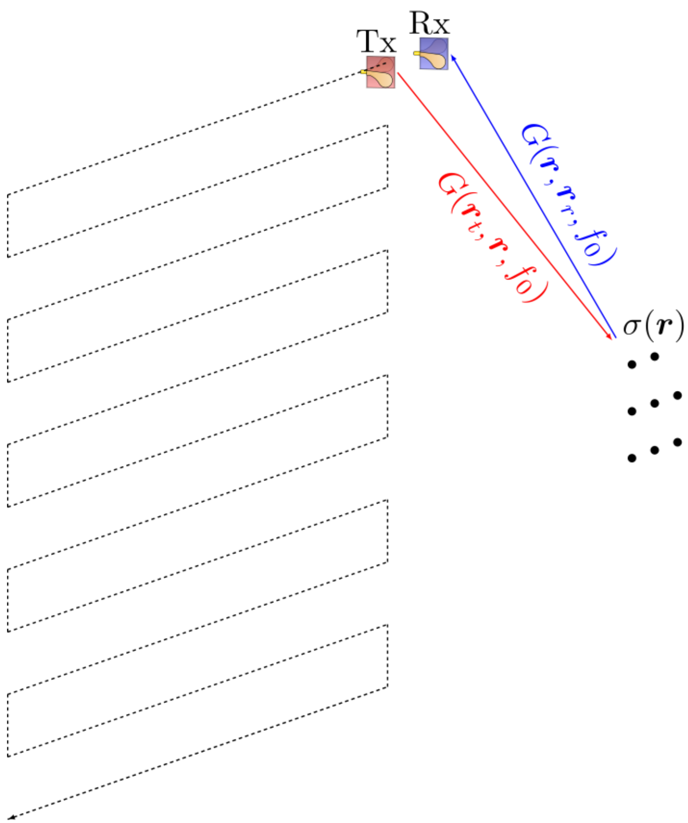

Expression of the measured signals

$$s(r_t, r_r) = \int_r G(r_t, r_r)\sigma(r)G(r, r_r)d^3r$$

Matrix formalism

$$s = H\sigma$$

Reconstruction by pseudo-inversion

$$\hat{\sigma} = H^+ s$$

Intensity measurement: Reflectivity reconstruction?

$$s_I = |s|^2 = |H\sigma|^2$$

Phaseless computational imaging

Intensity measurement: Reflectivity reconstruction?

$$s_I = |s|^2 = |H\sigma|^2$$

Solving an optimization problem

$$\underset{\boldsymbol{\sigma}}{\text{minimize}} \quad f(\boldsymbol{\sigma}) = \frac{1}{m}\sum_{i=1}^{m} |\langle h_i, \boldsymbol{\sigma}\rangle^2 - |s_i|^2| = ||(H\boldsymbol{\sigma})^2 - |\mathbf{s}|^2||_1$$

Convex programming

Example: CVX and Matlab

```
m = 20; n = 10; p = 4;
A = randn(m,n); b = randn(m,1);
C = randn(p,n); d = randn(p,1);
e = rand;
cvx_begin
    variable x(n)
    minimize( norm( A * x - b, 2 ) )
    subject to
    C * x == d
    norm( x, Inf ) <= e
cvx_end
```

Iterative algorithm

Example: Truncated Wirtinger Flow

$$\boldsymbol{y} = |\boldsymbol{A}\boldsymbol{x}|^2$$

$$\boldsymbol{x}^{(t+1)} = \boldsymbol{x}^{(t)} + \frac{\mu_t}{m}\sum_{i\in S_{t+1}}^{m} \nabla_{l_i}(\boldsymbol{x}^{(t)})$$

$$\nabla_{l_i}(\boldsymbol{x}^{(t)}) = 2\,\frac{\boldsymbol{y}_i - |\boldsymbol{a}_i^*\boldsymbol{x}^{(t)}|^2}{\boldsymbol{x}^{(t)*}\,\boldsymbol{a}_i}$$

where the adaptive index set S_{t+1} is determined by Chen and Candès satisfying for any $i \in S_t$:

$$\boldsymbol{a}_i^*\boldsymbol{x}^{(t)} \asymp ||\boldsymbol{x}^{(t)}||$$

$$\frac{\boldsymbol{y}_i - |\boldsymbol{a}_i^*\boldsymbol{x}^{(t)}|^2}{\boldsymbol{a}_i^*\boldsymbol{x}^{(t)}} \lesssim \frac{\frac{1}{m}|\boldsymbol{y}_i - |\boldsymbol{a}_i^*\boldsymbol{x}^{(t)}|^2|}{||\boldsymbol{x}^{(t)}||}$$

Candes, E. J., Li, X., & Soltanolkotabi, M. (2015). Phase retrieval via Wirtinger flow: Theory and algorithms. *IEEE Transactions on Information Theory*, *61*(4), 1985-2007.

Phaseless computational imaging

Experimental validation: SAR PhaseLess imaging

Aperture size: 60 × 60 cm^2
Number of samples: 61 × 61 = 3721
Background measurement (without marbles)

The results converge towards those obtained with phase measurement

Once again, the hardware constraint is transferred to the software layer

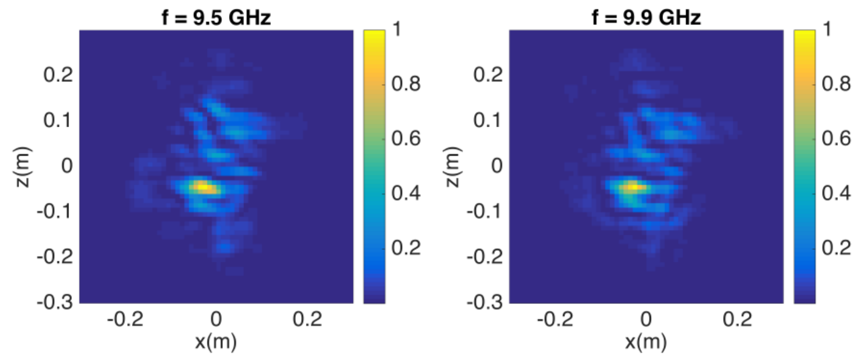

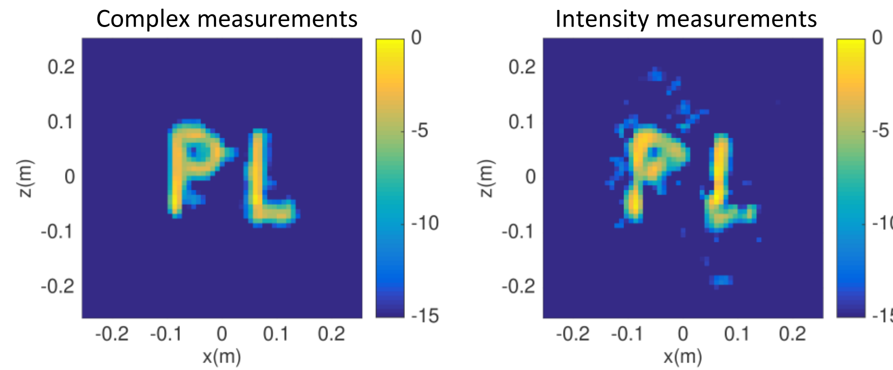

Phaseless computational imaging

Cavity-based phaseless localization

First step: localizing a source from an intensity measurement

The diversity of the magnitudes of near-field scans is the basis for encoding information

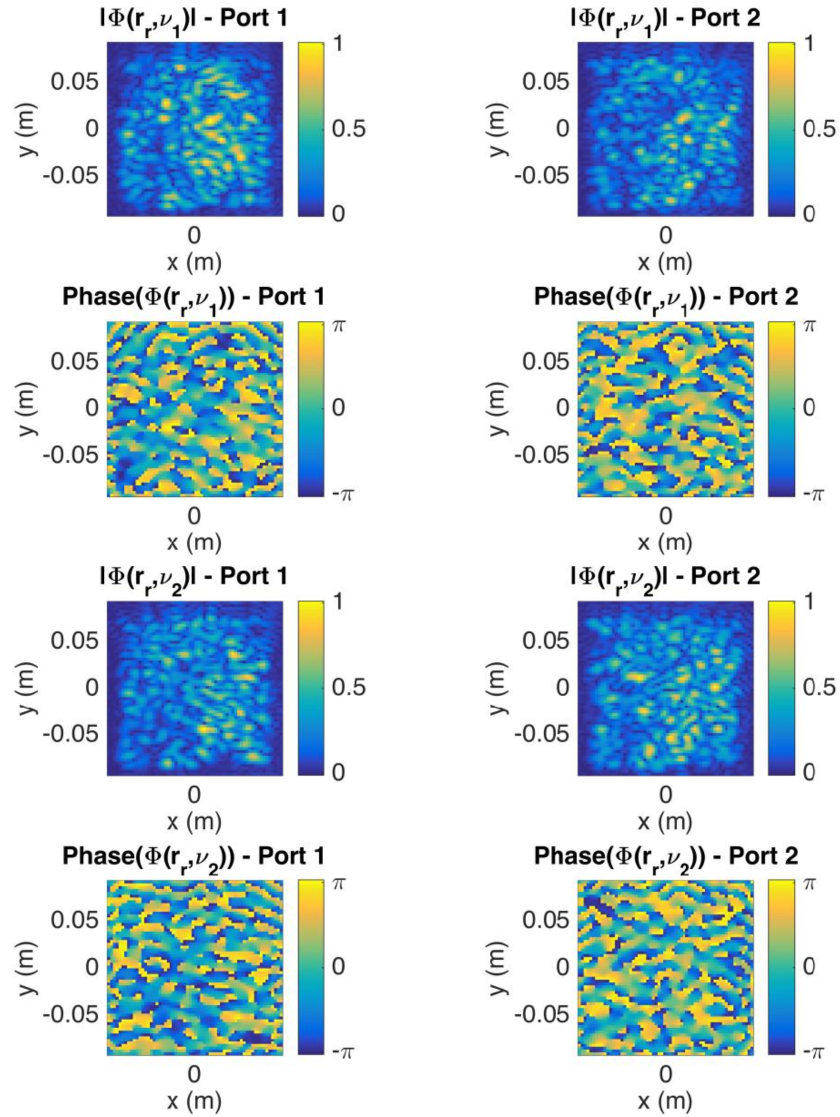

ν_1 = 23 GHz - ν_2 = 23.002 GHz

Fromenteze, T., Liu, X., Boyarsky, M., Gollub, J., & Smith, D. R. (2016). Phaseless computational imaging with a radiating metasurface. *Optics express*, *24*(15), 16760-16776.

Phaseless computational imaging

Cavity-based phaseless localization

First step: localizing a source from an intensity measurement

The diversity of the magnitudes of near-field scans is the basis for encoding information

Reconstruction from the measurement of two signals on the output ports of the cavity

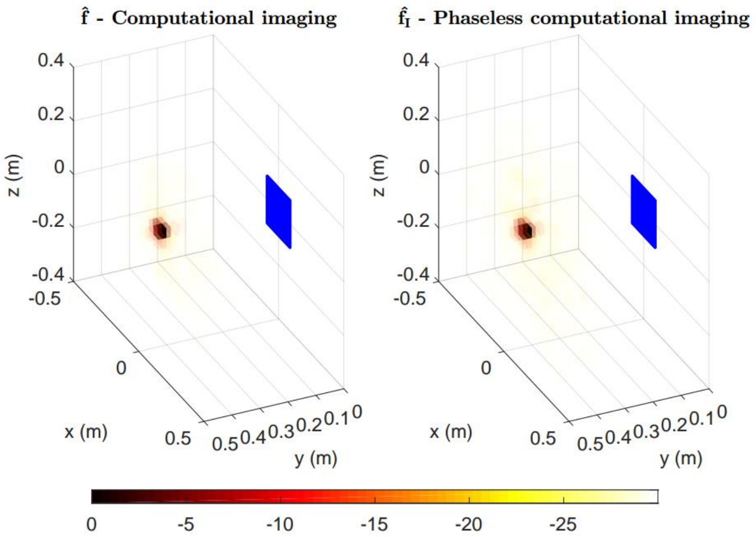

Algorithm: Truncated Wirtinger Flow
Number of spatial samples: 20 × 20 × 10
Number of frequency samples: 3601
Frequency range: 17.5-26.5 GHz

Fromenteze, T., Liu, X., Boyarsky, M., Gollub, J., & Smith, D. R. (2016). Phaseless computational imaging with a radiating metasurface. *Optics express*, *24*(15), 16760-16776.

Phaseless computational imaging

Cavity-based phaseless imaging

Switching to the interrogation of a reflectivity function

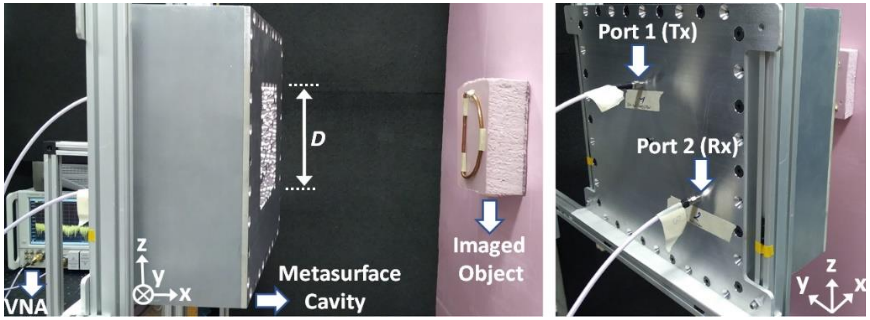

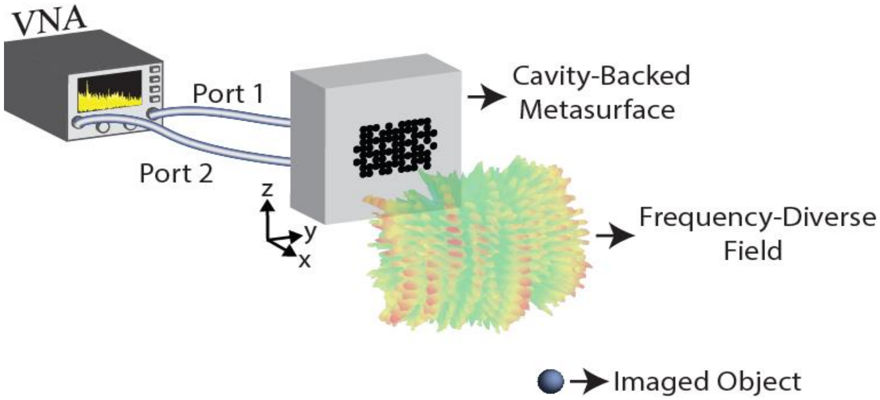

Small object for the determination of the point spread function

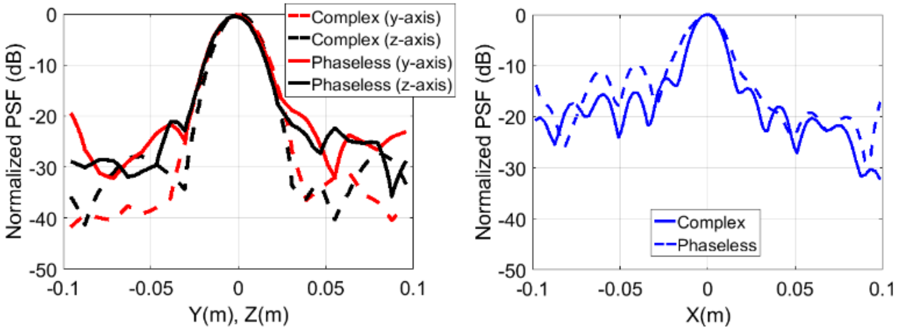

Use of a more advanced technique based on the sparsity of the scene to be imaged

Yuan, Z., Wang, H., & Wang, Q. (2019). Phase retrieval via sparse wirtinger flow. *Journal of Computational and Applied Mathematics*, *355*, 162-173.

Yurduseven, O., Fromenteze, T., Marks, D. L., Gollub, J. N., & Smith, D. R. (2017). Frequency-diverse computational microwave phaseless imaging. *IEEE Antennas and Wireless Propagation Letters*, *16*, 2808-2811.

Phaseless computational imaging

Cavity-based phaseless imaging

Switching to the interrogation of a reflectivity function

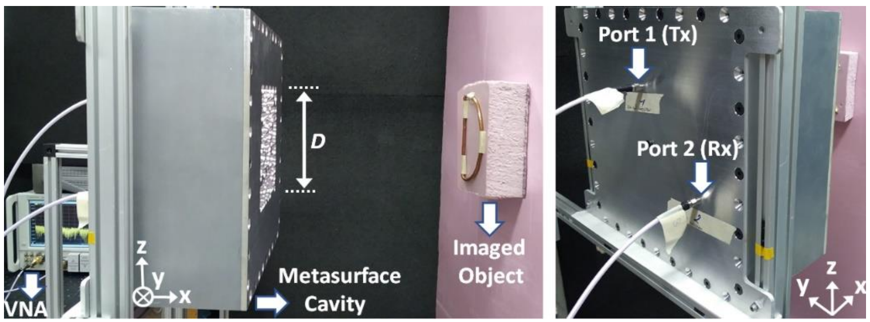

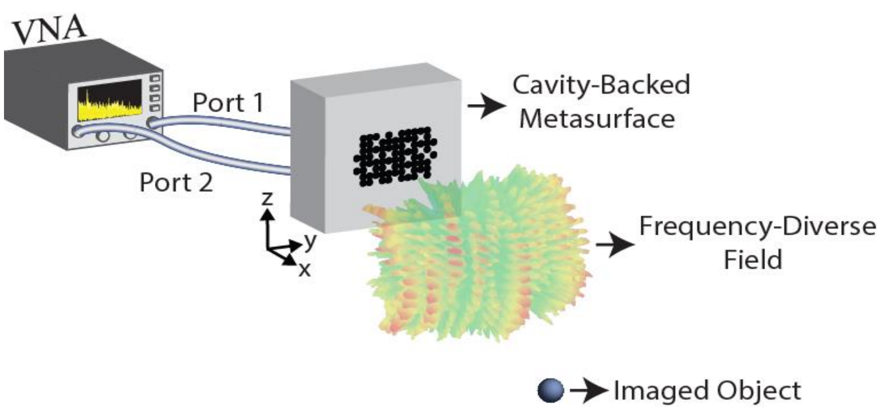

Key parameter: ratio M/N
M number of measurements
N number of voxels

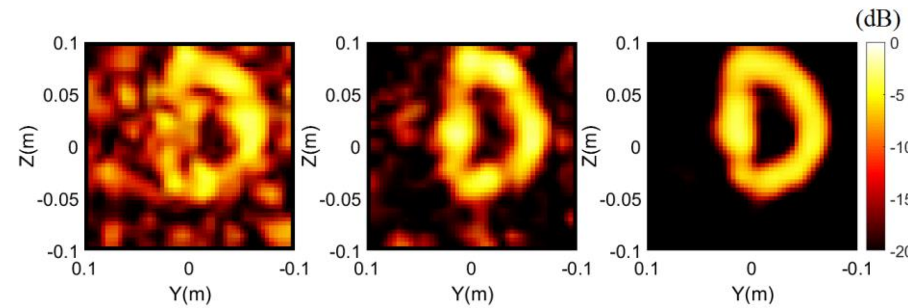

M/N = 0.3 M/N = 0.6 M/N = 0.8

Comparison of the performances achieved by the different approaches

Complex measurement | Sparse WF | Regular WF

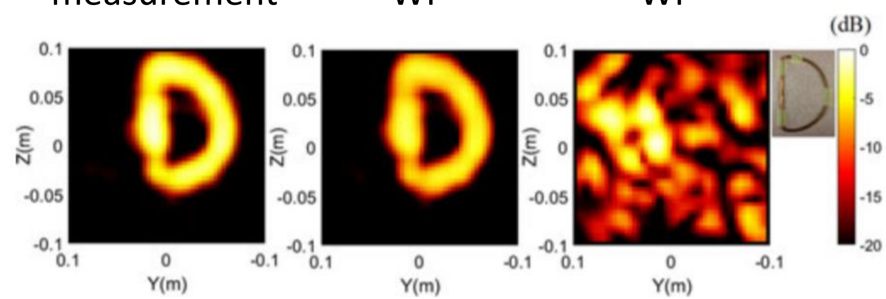

Yurduseven, O., Fromenteze, T., Marks, D. L., Gollub, J. N., & Smith, D. R. (2017). Frequency-diverse computational microwave phaseless imaging. *IEEE Antennas and Wireless Propagation Letters*, *16*, 2808-2811.

Phaseless computational imaging

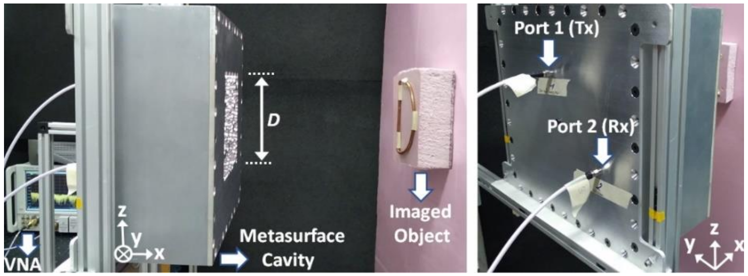

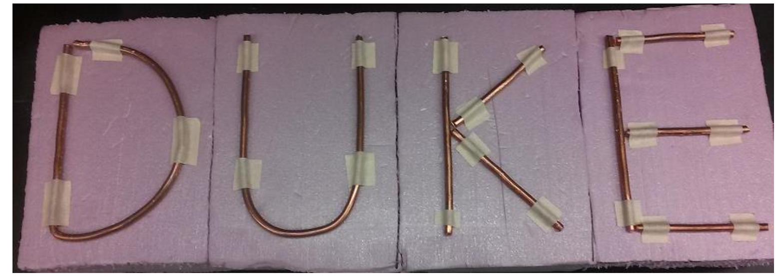

Complex-based reconstruction

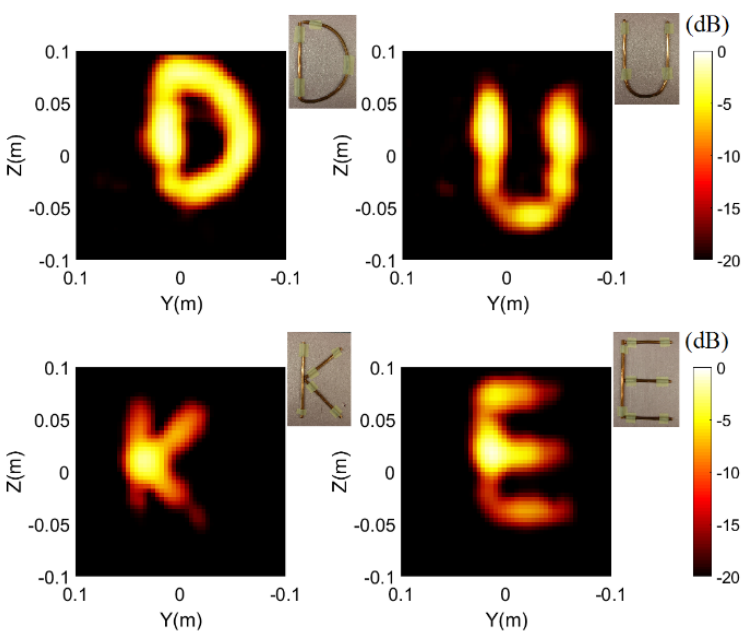

Phaseless reconstruction

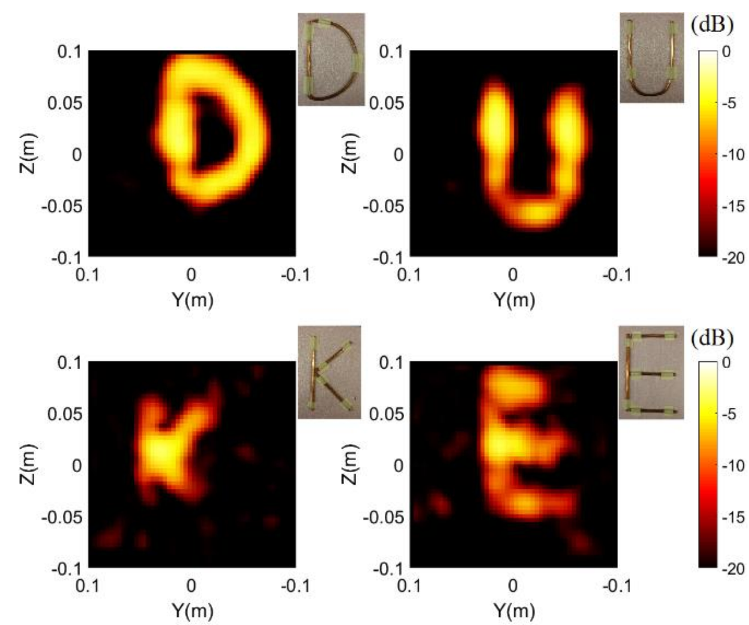

Yurduseven, O., Fromenteze, T., Marks, D. L., Gollub, J. N., & Smith, D. R. (2017). Frequency-diverse computational microwave phaseless imaging. *IEEE Antennas and Wireless Propagation Letters*, *16*, 2808-2811.

Phaseless computational imaging

Interesting feature of phaseless imaging:

relaxes the phase coherency requirements for applications where large apertures are needed

Without phase error

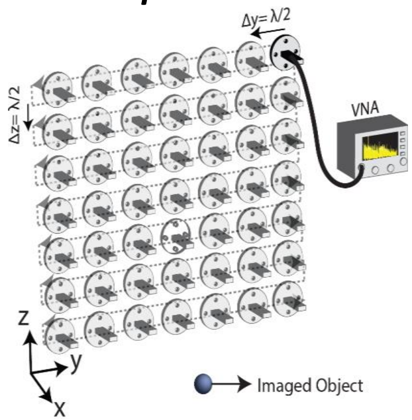

With phase error

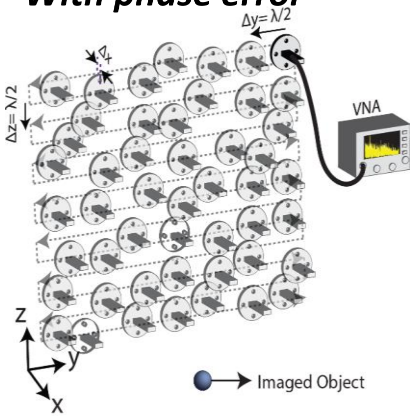

Complex-Based

Without phase error ***With phase error***

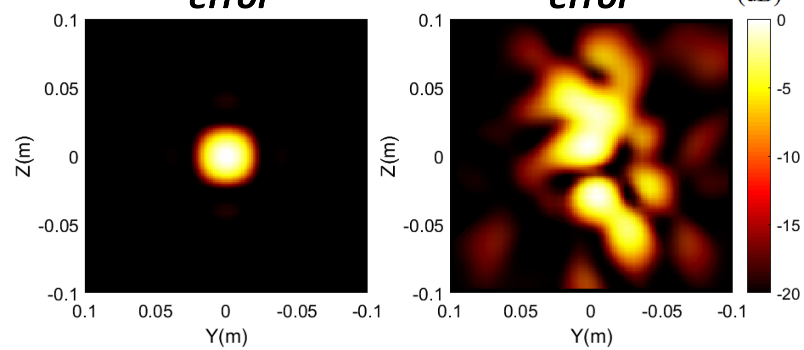

Phaseless

Without phase error ***With phase error***

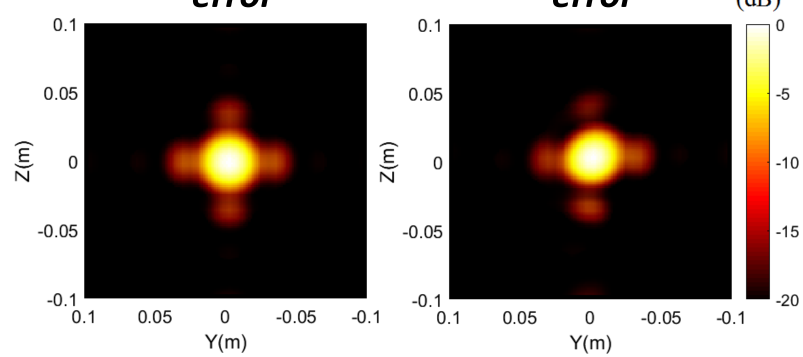

Yurduseven, O., Fromenteze, T., & Smith, D. R. (2018). Relaxation of alignment errors and phase calibration in computational frequency-diverse imaging using phase retrieval. *IEEE Access*, *6*, 14884-14894.

STh-01

MODERN ADVANCES IN COMPUTATIONAL IMAGING AT MICROWAVE AND MILLIMETRE-WAVE FREQUENCIES

Okan Yurduseven[#1], Thomas Fromentèze[#2]

[#1]Queen's University Belfast, UK

[#2]Xlim Research Institute, University of Limoges, France

[1]okan.yurduseven@qub.ac.uk, [2]thomas.fromenteze@unilim.fr